

## Chapter 20

### Growth and properties of hexagonal boron nitride (*h*-BN) based alloys and quantum wells

Q W Wang, J Li, J Y Lin and H X Jiang

#### 20.1 Introduction and unique properties of *h*-BN

Due to its extraordinary physical properties, layered structure, quasi-2D nature, and bandgap of about 6.5 eV, hexagonal boron nitride (*h*-BN) possesses promising rich novel properties. Currently, AlN is the best known deep UV semiconductor material with a comparable bandgap (~6.1 eV) to *h*-BN. Several unique features of *h*-BN in comparison to AlN are of immense interest for novel device exploration and can be summarized as follows.

*Ability to enable novel flexible devices with versatile form factors.* Significant progress in epitaxial growth using metal–organic chemical vapor deposition (MOCVD) for producing thick *h*-BN epilayers has been made in recent years [1–7]. When the thickness exceeds ~30 μm, after growth and during cooling down an *h*-BN epilayer tends to automatically separate from the sapphire substrate due to its unique hexagonal (layered) structure and the difference in thermal expansion coefficients between the *h*-BN and sapphire substrate [1–7]. As shown in figure 20.1, free-standing *h*-BN epilayers can be sliced into varying shapes and tiled together to form arrays, and are flexible with good conformability and transferability. Devices based on free-standing *h*-BN epilayers can be attached to rigid, flat, or curved surfaces. As such, these materials potentially offer a disruptive platform to design a wide range of photonic and electronic devices in flexible form factors.

*High optical emission efficiency.* As shown in figure 20.2(a), in comparison with AlN, the full width at half maximum (FWHM) of the x-ray diffraction (XRD) rocking curve of the *h*-BN (0002) diffraction peak is ~380 arcsec [8], which is 5–8 times broader than that of high quality AlN epilayers deposited on *c*-plane sapphire (around 60 arcsec) [9]. The FWHM of the XRD rocking curve of *h*-BN is comparable to those of typical GaN epilayers deposited on *c*-plane sapphire (around 290 arcsec) [10]. In III-nitride materials, it is well known that the FWHM of XRD

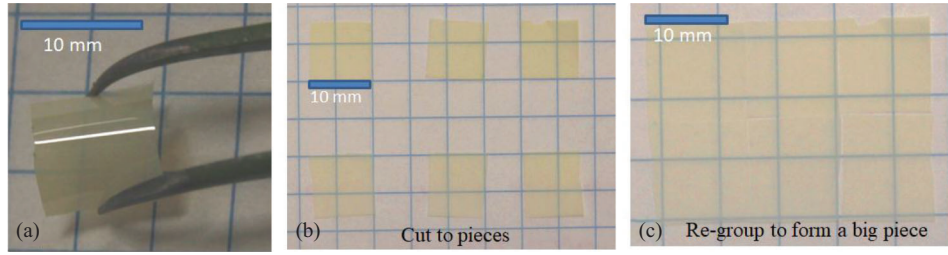


**Figure 20.1.** Optical images of free-standing (FS) *h*-BN epilayers of 50  $\mu\text{m}$  in thickness: (a) an FS *h*-BN epilayer displays flexibility, (b) an FS *h*-BN epilayer cut into small pieces, and (c) small pieces of FS *h*-BN epilayers grouped to form a large array.

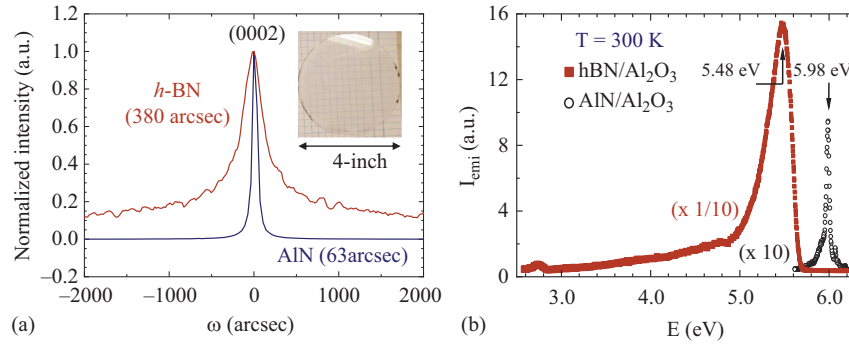


**Figure 20.2.** (a) Comparison of XRD rocking curves of the (0002) reflection peaks between *h*-BN and AlN epilayers (after [8]). (b) Comparison of DUV PL spectra between *h*-BN and AlN epilayers measured at 300 K (after [13] and [14]).

rocking curves is correlated with the density of dislocations [9–12]. In the case of *h*-BN with a layered structure, the FWHM could also reflect the presence of misalignment between layers, turbostratic (*t*-)phase layers, or variations in the *c*-plane orientation of individual layers within *h*-BN, stacking faults, and native and point defects. However, despite the fact that the crystalline quality of *h*-BN is poorer than that of AlN, the photoluminescence (PL) emission intensity of the band-edge transition in *h*-BN epilayers is generally more than two orders of magnitude higher than that of AlN epilayers with a comparable thickness [13, 14]. Note that the PL spectra shown in figure 20.2(b) are multiplied by a factor of 1/10 for *h*-BN and by 10 for AlN, respectively. These results imply that *h*-BN deep UV devices could potentially be even more efficient than AlN. This high emission efficiency is in part due to the quasi-2D nature of *h*-BN [13].

*TE versus TM mode.* It is well known that the band-edge emission in AlN and high Al-content AlGa<sub>N</sub> is dominated by the transverse-magnetic (TM) polarization mode due to the unique band structure of AlN [15, 16]. However, the TE mode is generally preferred for optoelectronic device applications because this mode allows for surface emitting light emitting diodes (LEDs) and is associated with a lower threshold and higher optical gain and lasing beam quality for laser diodes (LDs).

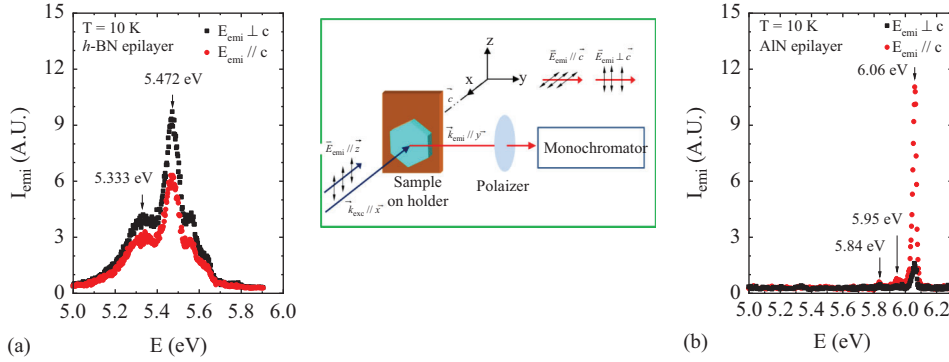


**Figure 20.3.** Comparison of polarization-resolved low temperature (10 K) band-edge PL spectra between (a) the *h*-BN epilayer and (b) AlN epilayer, with the emission polarization parallel ( $E_{\text{emi}}//c$ ) and perpendicular ( $E_{\text{emi}}\perp c$ ) to the *c*-axis (after [13] and [14]). The PL measurement configuration is depicted in the inset and the excitation laser line is polarized in the direction perpendicular to the *c*-axis ( $E_{\text{exc}}\perp c$ ).

Figure 20.3 compares the polarization-resolved band-edge PL emission spectra of *h*-BN and AlN epilayers measured at 10 K [13, 14]. The PL emission spectral lineshape for *h*-BN shown in figure 20.3(a) for the configuration with emission polarization along the crystal *c*-axis ( $E_{\text{emi}}//c$ ) is observed to be very similar to that in the ( $E_{\text{emi}}\perp c$ ) configuration. However, the emission intensity is about 1.7 times stronger in the ( $E_{\text{emi}}\perp c$ ) configuration, which is in sharp contrast to the polarization-resolved PL spectra of AlN shown in figure 20.3(b). However, the emission polarization of *h*-BN is the same as that of GaN [16–18]. The results clearly reveal that the band-edge emission in *h*-BN is predominantly transverse-electric (TE) polarized and agree with theoretical calculation results [13]. Due to the combination of the TE mode, large exciton binding energy, and 2D nature, *h*-BN light emitting devices are expected to be very efficient and *h*-BN based deep UV lasers should perform better than AlN based deep UV lasers.

**2D versus 3D.** Having a layered structure, *h*-BN is a quasi-2D material, whereas AlN is a 3D material. It was demonstrated that the strong optical transitions in *h*-BN partly originates from the unusually strong  $p \rightarrow p$ -like transitions due to its quasi-2D nature, giving rise to a very high density of states near the band edge [13]. Furthermore, the above band-edge optical absorption coefficient is around  $7 \times 10^5 \text{ cm}^{-1}$  for *h*-BN [19, 20] in comparison to  $2 \times 10^5 \text{ cm}^{-1}$  for AlN [21, 22]. This is also due to the quasi-2D nature of *h*-BN in which each layer absorbs 2.3% for the above bandgap photons [19].

**Improved *p*-type conductivity control over AlN.** Although Al-rich AlGa<sub>1-x</sub>N ternary alloys and AlN have been the default choice for the development of LEDs and LDs operating at wavelengths below 300 nm, the highly resistive nature of *p*-layers leads to very low hole injection efficiency and hence low quantum efficiency (QE). The poor *p*-type conductivity of Al-rich Al<sub>x</sub>Ga<sub>1-x</sub>N alloys is the major obstacle that limits the QE of deep ultraviolet (DUV) light emitting devices. This problem is due to the deepening of the Mg acceptor level in Al<sub>x</sub>Ga<sub>1-x</sub>N with increasing *x*, from about 170 meV ( $x = 0$ ) to 530 meV ( $x = 1$ ) [23–26]. Since the free hole concentration

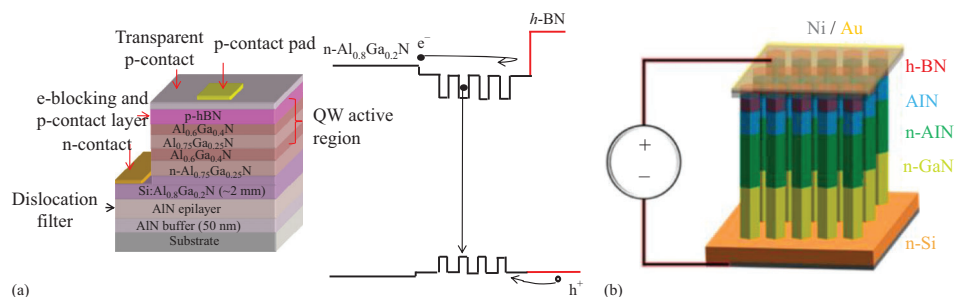


**Figure 20.4.** (a) Schematic of a DUV LED layer structure incorporating p-type *h*-BN. The wide bandgap p-type *h*-BN serves as a natural electron-blocking (e-blocking), hole injection and p-type contact layer. The approach is based on *h*-BN's unique band-edge alignment with AlGa<sub>N</sub>, improved p-type conductivity over AlN and transparency to DUV photons (after [23] and [29]). (b) A 210 nm deep UV LED fabricated from p-type *h*-BN/*n*-AlN nanowire heterostructure. Reproduced with permission from [30]. Copyright 2017 American Chemical Society.

depends exponentially on the acceptor energy level ( $E_a$ ), an  $E_a$  value around 500 meV translates to only 1 free hole for roughly every 2 billion ( $2 \times 10^9$ ) incorporated Mg impurities (at 300 K). This causes an extremely low free hole injection efficiency into the quantum well (QW) active region and is a major obstacle for the realization of high-performance AlGa<sub>N</sub>-based DUV emitters. Significant advances in the QE of DUV emitters will require the exploitation of disruptive device concepts. It was shown that a much lower p-type resistivity can be achieved in *h*-BN than in AlN. A p-type resistivity of  $\sim 2 \Omega \text{ cm}$  at 300 K by Mg doping has been demonstrated in *h*-BN [23, 27, 28], which is about five to six orders of magnitude lower than what has been possible for Mg doped AlN ( $> 10^5 \Omega \text{ cm}$ ) [24]. A p-BN/*n*-AlGa<sub>N</sub> heterostructure, as schematically shown in figure 20.4(a) [23, 29], has been explored for deep UV device applications and can be further improved to tackle the p-type conductivity issue in DUV emitters based on high Al-content AlGa<sub>N</sub>. More recently, very promising results have been demonstrated for AlGa<sub>N</sub> nanowire based DUV LED structures, as illustrated in figure 20.4(b), by utilizing *h*-BN as a p-type current injection layer [30].

*Huge exciton binding energy.* The calculated exciton binding energy in 2D *h*-BN is huge and ranges from 0.71 to 0.76 eV [13, 31–33]. Experimentally, from the temperature dependence of the exciton decay lifetime, an exciton binding energy of  $\sim 740 \text{ meV}$  and a small exciton Bohr radius of  $\sim 8 \text{ \AA}$  have been indirectly deduced [34]. Photocurrent excitation spectroscopy has also been utilized to directly probe the fundamental band parameters of *h*-BN. As shown in figure 20.5(a), transitions in a photoexcitation spectrum obtained at a fixed bias voltage corresponding to the direct band-to-band, free excitons, and impurity bound excitons have been directly observed. From the observed transition peak positions, the room temperature bandgap ( $E_g \sim 6.42 \text{ eV}$ ) and binding energy of excitons ( $E_x \sim 0.73 \text{ eV}$ ) were directly measured and a band diagram has been constructed as shown in figure 20.5(b) [35]. This exciton binding energy is about one order of magnitude larger than the well-known very large exciton binding energy in AlN [36–39] and is likely the largest

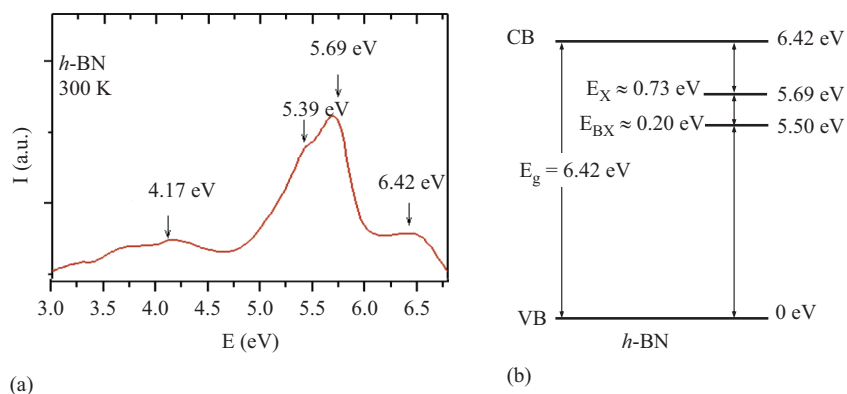


**Figure 20.5.** (a) Room temperature photocurrent excitation spectrum of a metal–semiconductor–metal detector consisting of micro-strip interdigital fingers ( $6 \mu\text{m}/9 \mu\text{m}$  of width/spacing) fabricated from an  $h$ -BN epilayer measured at a bias voltage = 100 V applied between detector fingers. (b) Energy band diagram including the room temperature energy bandgap ( $E_g$ ), the binding energy of a free exciton ( $E_x$ ), and the binding energy of an impurity bound exciton ( $E_{bx}$ ) in  $h$ -BN epilayers constructed from the photocurrent excitation spectrum shown in (a), neglecting possible effects due to strain (after [35]).

in inorganic 2D semiconductors. This huge binding energy is expected to have large consequences on its applications as light emitting devices.

*Low electron affinity.*  $h$ -BN has a very low or even negative electron affinity, similar to diamond and appears to be promising as a high-performance electron emitter material with potential advantages of high power/power density and low transverse emissivity [20].

*Ideal material for  $h$ -BN/graphene heterostructure applications.* Due to its similar in-plane lattice constant to graphene and chemical inertness and resistance to oxidation,  $h$ -BN has been established as an ideal material for the exploration of van der Waals heterostructures and devices with new physics and applications [40–43].

*Possible host for single photon emitters.* More recently,  $h$ -BN has emerged as a promising material to host single photon emitters. More specifically, room temperature stable single photon emissions in a broad spectral range from about 1.65 to 2.2 eV have been observed in tape exfoliated  $h$ -BN multilayers as well as in small  $h$ -BN powder and bulk crystals [44–50]. In contrast to the well-studied diamond material, in which it is generally accepted that NV centers are the origin of single photon emitters, the physical origin of single photon emitters in  $h$ -BN is still a topic of experimental and theoretical debate [44–51].

*Material of choice for solid-state neutron detectors.* As shown in figure 20.6(a), the isotope B-10 is among a few isotopes that can interact with neutrons with a large capture cross-section (only second to  $^3\text{He}$ ) and has a capture cross-section of about 3840 barns for thermal neutrons (neutrons with an average energy = 25 meV) [52]. As a semiconductor, the density of B atoms in 100%  $^{10}\text{B}$ -enriched BN which can interact with thermal neutrons is  $5.5 \times 10^{22}/\text{cm}^3$ , which is about 550 times higher than that in He-3 gas pressurized at 4 atm [1]. This unique property makes  $h$ -BN a

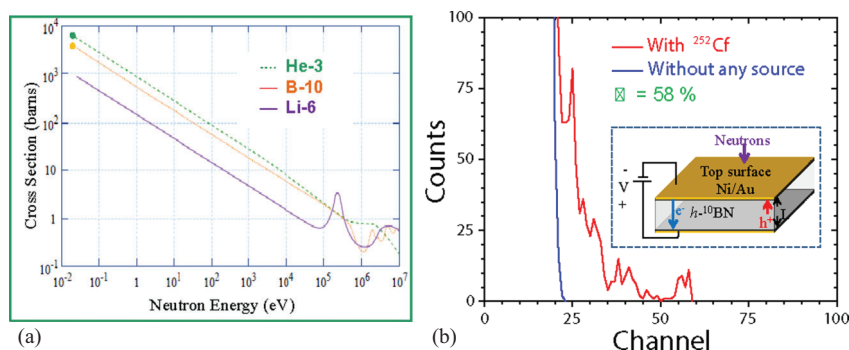


**Figure 20.6.** (a) Neutron capture cross sections as functions of the kinetic energy of neutrons for He-3, B-10, and Li-6. The green and orange dots indicate, respectively, the cross sections in He-3 and B-10 for thermal neutrons (neutrons with an average energy of 0.025 eV). (b) Nuclear reaction pulse height spectrum of a B-10 enriched *h*-BN detector with the device configuration shown in the inset under thermal neutron radiation. The neutron response was measured by placing the detector at 30 cm away from the <sup>252</sup>Cf source moderated by a one-inch thick high-density polyethylene (HDPE) moderator at a bias voltage of 200V for 15 min. Reproduced with permission from [3]. Copyright 2018 AIP Publishing.

highly promising material for the fabrication of solid-state neutron detectors [1–7]. As illustrated in figure 20.6(b), the recent achievement of free-standing B-10 enriched *h*-BN epilayers of large thicknesses ( $> 50 \mu\text{m}$ ) has enabled the realization of thermal neutron detectors with an unprecedented record high detection efficiency among all solid-state detectors at 58% [3, 6]. In comparison to He-3 gas detectors, BN neutron detectors possess all the intrinsic advantages of semiconductor devices: light weight, compact size, fast response speed, ease of mass production via utilization of existing semiconductor manufacturing infrastructures, low cost for operation and maintenance, flexible form factors, and durability. The price of He-3 gas is also very high because He-3 gas is extremely rare on Earth. Neutron detectors have applications in many industries including special nuclear material tracking, nuclear hazard detection, life (water) searching in space, and geothermal and well logging. Other potential applications of neutron detectors include neutron scattering experiments for materials research, neutron cameras for neutron radiography for monitoring metal structures and parts, and for medical applications such as neutron imaging and boron neutron capture therapy for cancer treatment.

Despite its unique combination of superb properties, as with all other compound semiconductors, achieving the ability to tune the optoelectronic properties through alloying and heterojunction formation is highly desirable and will further expand the usefulness of *h*-BN. One way to achieve bandgap engineering in *h*-BN is to form alloys with GaN, namely  $\text{Ga}_x\text{B}_{1-x}\text{N}$  alloys [53, 54]. Despite the fact that the equilibrium phases of GaN and BN are wurtzite and hexagonal, respectively, recent theoretical studies indicated that a 2D hexagonal layered structure is thermodynamically the most stable structure for few-layer nitride semiconductors (GaN, AlN, InN) [55–57] and the transition from layered structure to wurtzite structure occurs at eight layers for InN, ten for GaN, and 22 for AlN in the absence of strain [56]. An alternative approach to realizing *h*-BN based alloys is to consider the layer-

structured hexagonal boron nitride carbon semiconductor alloys,  $h$ -(BN)C [58–61]. Both  $h$ -BN and graphite (C) are layer-structured materials with similar lattice parameters and crystalline structures. The in-plane  $a$ -lattice constant difference is only about 1.5% between graphite and  $h$ -BN. The  $h$ -(BN) $_{1-x}$ (C $_2$ ) $_x$  alloy system thus holds the unique advantages of identical crystalline structure (hexagonal) and excellent matches in lattice constants, thermal expansion coefficients, and melting points throughout the entire alloy range. In this chapter, we summarize recent progress made in terms of MOCVD growth and the understanding of the basic properties of hexagonal (BN)C and BGaN alloys and heterostructures.

## 20.2 Prospects of $h$ -BN-based alloys and heterostructures

With the recent progress in achieving  $h$ -BN at the wafer-scale using MOCVD growth, we are now provided with an ideal template to expand the epitaxial growth technique to produce novel 2D layer-structured  $h$ -BCN and  $h$ -BGaN alloys, heterostructures, and QWs. These new material systems are expected to possess different properties from bulk or epilayer structures with respect to the energy bandgaps, 2D transport and optical properties. Some of the basic properties that can be envisioned from  $h$ -BGaN based alloys include the following.

*Bandgap variation in 2D semiconductors.* The energy bandgap variations of these alloy systems are expected to be very large. Both hexagonal boron nitride ( $h$ -BN) and graphite (C) are layered materials with similar lattice parameters and crystalline structures. The in-plane  $a$ -lattice constant difference is only about 1.5% between graphite and  $h$ -BN, which provides the potential to synthesize layer-structured  $h$ -(BN) $_{1-x}$ (C $_2$ ) $_x$  alloys. The  $h$ -(BN) $_{1-x}$ (C $_2$ ) $_x$  alloy system thus holds the unique advantages of identical crystalline structure (hexagonal) and excellent matches in lattice constants, thermal expansion coefficients, and melting points throughout the entire alloy range. Moreover, as schematically shown in figure 20.7(a), this layer-structured alloy system potentially possesses an extremely large energy gap ( $E_g$ ) variation from around 6.5 eV for  $h$ -BN to 0 for graphite. From an electrical properties perspective, this alloy system provides a large range of conductivity control from highly resistive semiconductors (undoped  $h$ -BN) to semi-metal (graphite). The  $h$ -(BN) $_{1-x}$ (C $_2$ ) $_x$  alloys in the BN-rich side would complement III-nitride wide bandgap semiconductors as a layer-structured material system functioning in the deep UV spectral region. The  $h$ -(BN) $_{1-x}$ (C $_2$ ) $_x$  alloys in the C-rich side have the potential to provide an unprecedented degree of freedom in the design of infrared (IR) detector and electronic devices. More specifically, the bandgap energy tunability in the C-rich side could offer IR detectors with cut-off wavelengths from the short wavelength IR (SWIR: 1–3  $\mu$ m) to very long wavelength (VLWIR: 14–30  $\mu$ m) range. Furthermore, C-rich  $h$ -(BN) $_{1-x}$ (C $_2$ ) $_x$  alloys would address the major challenges facing the emerging 2D materials and open up new realms for novel physical properties and device exploration. On the other hand, with the energy gaps of  $h$ -BN and  $h$ -GaN of around 6.5 eV [34, 35] and 4.5 eV [62], respectively, this layer-structured  $h$ -BGaN alloy system appears to offer a large bandgap variation.

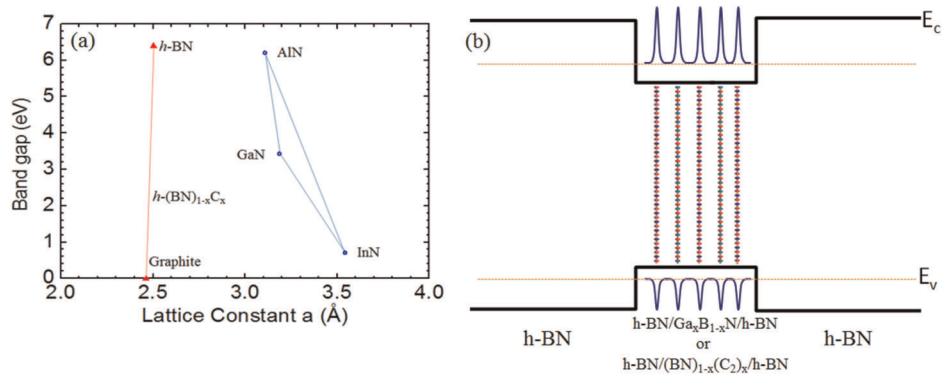


**Figure 20.7.** (a) Comparison of the energy bandgap variation of the  $a$ -lattice constant of  $h$ -(BN)C alloys with InGaAlN alloys. (b) Schematic of the band structure of a  $h$ -BN/ $h$ -Ga $_x$ B $_{1-x}$ N/ $h$ -BN or  $h$ -BN/ $h$ -(BN) $_{1-x}$ (C $_2$ ) $_x$ / $h$ -BN QW with five well layers of  $h$ -Ga $_x$ B $_{1-x}$ N or  $h$ -(BN) $_{1-x}$ (C $_2$ ) $_x$ , in which carriers are confined in the  $h$ -Ga $_x$ B $_{1-x}$ N or  $h$ -(BN) $_{1-x}$ (C $_2$ ) $_x$  layers in addition to the confinement provided by  $h$ -BN barriers.

The system also offers the possibility for conductivity control from the highly insulating semiconductor (undoped  $h$ -BN) to conductive GaN and therefore potentially enables the possibility of monolithic integration of the active layer, carrier injection layers, dielectric layer, and passivation layers via a single growth process.

*Unique heterostructures and QWs.* In  $h$ -BN/ $h$ -Ga $_x$ B $_{1-x}$ N/ $h$ -BN and  $h$ -BN/ $h$ -(BN) $_{1-x}$ (C $_2$ ) $_x$ / $h$ -BN QWs, excitons are confined in the layers in addition to the confinement provided by  $h$ -BN barriers, as schematically illustrated in figure 20.7(b). This unique property stems from the fact that the wavefunctions of electrons and holes in these QWs do not extend through the whole well region as in those conventional QWs, since carriers and excitons are confined in the layers and there is a large potential barrier between layers. This naturally occurring large quantum confinement may significantly enhance the collective dipole interaction between the excitons and photon fields in micro-size cavities.

*Possibility for novel detector structures.* For 2D layered structures, a single layer or a few layers are adequate for many applications. However, for certain applications such as photodetectors, tens of layers may be needed. Other than the quantum confinement effects resulting from these layered QWs,  $h$ -BN can also be used as separation layers for a single layer or a few layers of  $h$ -(BN) $_{1-x}$ (C $_2$ ) $_x$  and  $h$ -BGaN by recognizing the fact that each layer only absorbs 2.3% of incoming light with energies above its bandgap. Due to the capability for bandgap engineering via alloying, if successfully realized, these structures have the potential to serve as a basic building blocks for the construction of emitters and detectors operating from the DUV to FIR and THz, full spectrum solar cells, and multi-spectral detectors.

*Possibility for novel laser structures.* Due to the photon–exciton interaction in semiconductors, there arise new elementary excitations, which are essentially mixed states of the photon and exciton: excitonic-polaritons. Polaritons can be utilized to design polariton lasers. In contrast to conventional semiconductor lasers, polariton

lasers have very low threshold current because polariton lasing involves only the spontaneous emission of coherent light of an exciton–polariton condensate and does not rely on population inversion. In recent years, there has been intense interest in understanding polaritons and developing room temperature polariton lasers using wide bandgap semiconductors [63, 64]. In wide bandgap semiconductors, the exciton binding energy and oscillator strength are large enough such that polariton condensation and lasing at visible to ultraviolet wavelengths can survive at 300 K. Due to a very strong collective dipole interaction between the QW excitons and microcavity photon fields, even with a relatively low- $Q$  cavity, the planar microcavity system is expected to feature a reversible spontaneous emission and thus normal-mode splitting into upper and lower branches of polaritons, spectrally separated by the Rabi splitting energy  $\hbar\Omega$ . The exciton oscillator strength  $f$  is written as

$$f = \frac{2m^*\omega}{\hbar} |\langle u_v | r \cdot e | u_c \rangle|^2 \frac{V}{\pi a_B^3}. \quad (20.1)$$

Here  $m^* = (m_e^{-1} + m_h^{-1})^{-1}$  is the effective mass of the exciton,  $m_e$  ( $m_h$ ) is the effective mass of the electron (hole),  $\omega$  is the frequency of photons,  $|u_c\rangle$  and  $|u_v\rangle$  are the electron and hole Bloch wavefunctions,  $V$  is the quantization volume, and  $a_B$  is the Bohr radius of the exciton. The binding energy ( $E_B$ ) of the ground exciton state is

$$E_B = \frac{e^2}{2\epsilon a_B} \text{ or } E_B = \frac{h^2}{\pi^2 \mu a_B^2}, \quad (20.2)$$

where  $\epsilon$  is the crystal's dielectric constant,  $e$  is the electron electric charge,  $h$  is Planck's constant,  $\mu$  is the exciton reduced mass  $\mu = \epsilon m_o a_o / a_B$ ,  $a_o = 0.53 \text{ \AA}$  is the Bohr radius of the hydrogen atom, and  $m_o$  is the mass of free electron. The ratio  $V/\pi a_B^3$  reflects the oscillator strength enhancement due to enhanced electron–hole overlap in an exciton compared to an unbound electron and hole pair. This ratio is very large, i.e. the exciton oscillator strength is much larger in wide bandgap semiconductors which have larger exciton binding energies or smaller exciton Bohr radii than those in small bandgap semiconductors. The exciton binding energy of about 740 meV in  $h$ -BN is at least one order of magnitude larger whereas the exciton Bohr radius of  $\sim 8 \text{ \AA}$  in  $h$ -BN is much smaller than those in the other well-known wide bandgap semiconductors, GaN, ZnO, and AlN. It is further noted that the predicted exciton binding energy in a single  $h$ -BN layer (or  $h$ -BN single sheet) is as large as 2.1 eV [32]. Moreover,  $h$ -BN is also a natural hyperbolic material with a strong uniaxial anisotropy, in which the transverse and longitudinal permittivities (the real parts) have opposite signs [65] and hence it is likely to enable many novel applications. However, developing  $h$ -BN based alloys and QWs structures such as those shown in figure 20.7(b) is necessary to enable carrier injection from the barrier into the well regions and practical current injection devices.

### 20.3 Epitaxy growth and properties of *h*-BGaN alloys and QWs

BGaN and BAlN in the wurtzite (WZ) phase have attracted considerable interest for UV material and device applications, as these alloys potentially offer the ability of tuning the bandgap energy from the blue to deep UV spectral region as well as providing an improved lattice match with SiC substrates [66–69]. Significant progress has been made recently in realizing  $B_xAl_{1-x}N$  epitaxial layers in single WZ phase by MOCVD [70, 71]. Similarly, a majority of theoretical studies have also focused on the WZ phase BGaN and BAlN alloys [72–74].

Theoretical and experimental studies on the synthesis and structural stability of BGaN alloys in the hexagonal phase are scarce. Most recently, an empirical bond-order potential (BOP) with the aid of *ab initio* calculations has been applied to investigate the structures and miscibility of  $B_xAl_{1-x}N$  and  $B_xGa_{1-x}N$  alloys [75, 76]. Table 20.1 shows the calculated equilibrium bond length  $r_e$  and the cohesive energy  $E_{\text{coh}}$  of BN and GaN for free-standing hexagonal (Hex), wurtzite (WZ), and zinc blende (ZB) structures. Figure 20.8(a) shows the cohesive energy differences between

**Table 20.1.** Calculated cohesive energy  $E_{\text{coh}}$  and equilibrium bond length  $r_e$  for Hex, WZ, and ZB structures in BN and GaN. Adapted from [76]. Copyright 2019 The Japan Society of Applied Physics.

Material	Structure	$E_{\text{coh}}$ (eV atom <sup>-1</sup> )	$r_e$ (Å)
BN	Hex	-6.944	1.48
	WZ	-6.796	1.57
	ZB	-6.813	1.57
GaN	Hex	-4.261	1.90
	WZ	-4.677	1.96
	ZB	-4.673	1.96

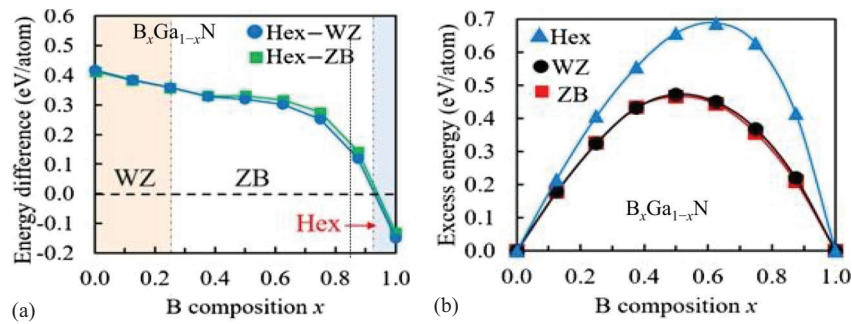


**Figure 20.8.** (a) Cohesive energy difference with respect to the cohesive energy of the hexagonal (Hex) structure for  $B_xGa_{1-x}N$  alloys as a function of boron composition,  $x$ . Positive values indicate that the wurtzite (WZ) and zinc blende (ZB) structures are more stable than the Hex structure. (b) Excess energy of  $B_xGa_{1-x}N$  alloys as a function of boron composition,  $x$ . The triangle, circle, and squares represent the excess energies of the Hex, WZ, and ZB structures. Reproduced with permission from [76]. Copyright 2019 The Japan Society of Applied Physics.

Hex and WZ structures as well as between Hex and ZB structures for  $B_xGa_{1-x}N$  alloys as functions of boron composition  $x$ . The energy differences were calculated using  $\Delta E(\text{Hex-WZ}) = E(\text{Hex}) - E(\text{WZ})$  and  $\Delta E(\text{Hex-ZB}) = E(\text{Hex}) - E(\text{ZB})$ , where  $E(\text{Hex})$ ,  $E(\text{WZ})$ , and  $E(\text{ZB})$  denote the cohesive energies of alloys with Hex, WZ, and ZB structures, respectively. As shown in figure 20.8(a), the calculated energy differences are positive for boron compositions  $<0.93$ , meaning that the formation of  $B_xGa_{1-x}N$  alloys in the hexagonal phase in the range of boron compositions less than 0.93 (or Ga compositions greater than 7%) is energetically unfavorable. However, figure 20.8(a) shows that the calculated energy differences sharply become negative values and clearly revealed that for the boron composition  $\geq 0.93$  (or for Ga compositions  $\leq 7\%$ ) the hexagonal structure can be stabilized in free-standing (BN)-rich BGaN alloys [75, 76]. The authors attributed this effect to the small energy difference among Hex, WZ, and ZB structures in BN of  $\sim 0.13$  eV atom<sup>-1</sup>. Figure 20.8(b) shows the calculated excess energy  $\Delta E_{\text{ex}}$  of the  $B_xGa_{1-x}N$  alloy as a function of boron composition  $x$ , where the excess energy of the  $B_xGa_{1-x}N$  alloy is given by  $\Delta E_{\text{ex}} = E(B_xGa_{1-x}N) - \{xE(\text{BN}) + (1-x)E(\text{GaN})\}$ . The calculated excess energies of  $B_xGa_{1-x}N$  alloys in WZ and ZB structures, shown in figure 20.8(b), are lower than those in Hex structure. The calculation results shown in figure 20.8(b) therefore indicate that the miscibility of  $B_xGa_{1-x}N$  alloys with hexagonal structure is lower than that with WZ and ZB structures due to the relaxation of atoms within in-plane directions in the hexagonal structure. In particular, the calculation results revealed that the ZB structure tends to stabilize over a wide boron composition range for  $B_xGa_{1-x}N$  alloys [75, 76].

Experimentally, it has been observed that a few layers of ZnO grown on Ag(111) substrates indeed crystallize into a graphitic or hexagonal BN (*h*-BN) structure instead of the equilibrium wurtzite structure [77]. The synthesis of 2D GaN has been recently demonstrated via a migration-enhanced encapsulated growth technique utilizing epitaxial graphene [62]. However, the hexagonal phase has not been experimentally observed in free-standing III-nitride semiconductors (AlN, GaN, InN, and their alloys) or deposited on a substrate prior to recent works [53, 54]. Epitaxial growth of hexagonal phase (BN)-rich  $Ga_xB_{1-x}N$  alloys (*h*- $Ga_xB_{1-x}N$ ) has been attempted only recently via an MOCVD technique by utilizing the *h*-BN epilayer as a template to promote the crystallization of BGaN alloys into the hexagonal phase [53, 54]. The results presented in the sub-sections below are based on these recent published results.

### 20.3.1 Epitaxial growth of *h*- $Ga_xB_{1-x}N$ alloys

For the epitaxial growth of hexagonal phase (BN)-rich  $Ga_xB_{1-x}N$  alloys by MOCVD, triethylboron (TEB), ammonia (NH<sub>3</sub>), and trimethylgallium (TMGa) were used as precursors for B, N, and Ga, respectively, and hydrogen as a carrier gas [53]. Prior to the deposition of *h*-BGaN, a 10 nm thick *h*-BN epilayer was first deposited on *c*-plane sapphire substrate at 1300 °C to serve as a template. Because GaN tends to decompose above 1200 °C, a growth temperature of 1225 °C was chosen for *h*-BGaN alloys in order to accommodate the incorporation of Ga while

retaining a reasonable crystalline quality. The alloy composition was controlled via the variation of the TMGa flow rate ( $R_{\text{TMG}}$ ) while keeping both the TEB and  $\text{NH}_3$  flow rates constant.

The XRD  $\theta$ - $2\theta$  scans for  $h$ -BGaN alloys grown under different TMGa flow rates ( $R_{\text{TMG}}$ ) shown in figure 20.9(a) all exhibit diffraction peaks near  $26^\circ$ , which are close to that of the  $h$ -BN (0002) diffraction peak. The results thus confirmed that these alloys have been crystallized into the hexagonal phase. Consequently, the corresponding  $c$ -lattice constants of  $h$ -BGaN alloys can be calculated based on the measured  $\theta$ - $2\theta$  peak positions as summarized in figure 20.9(b), revealing an onset point occurring at  $R_{\text{TMG}} = 4$  sccm. Figure 20.9(b) indicate that the  $c$ -lattice constant of  $h$ -BGaN increases from  $6.85 \text{ \AA}$  to  $6.94 \text{ \AA}$  as  $R_{\text{TMG}}$  was increased from 0 to 4 sccm. No further increase in the  $c$ -lattice constant was noticeable when  $R_{\text{TMG}}$  was increased beyond 4 sccm. As the theoretically calculated  $a$ -lattice constant of single layer  $h$ -GaN is  $a = 3.21 \text{ \AA}$  [2],  $h$ -BGaN epilayers grown on  $h$ -BN templates are expected to undergo a compressive strain. Therefore, an increase in the inter-plane distance ( $c/2$ ) is expected with the incorporation of Ga. Moreover, it interesting to note in figure 20.9(b) that the XRD  $\theta$ - $2\theta$  peak intensity as a function of TMGa flow rate ( $R_{\text{TMG}}$ ) exhibits an initial rapid decrease followed by almost no change, with the onset point also occurring at  $R_{\text{TMG}} = 4$  sccm, corroborating the dependence of the  $c$ -lattice constant on  $R_{\text{TMG}}$ .

Since XRD  $\theta$ - $2\theta$  scans provide information concerning the  $c$ -lattice constants and there are no available data for the  $c$ -lattice constant of  $h$ -GaN, the well-established Vegard's law cannot be applied to determine the composition of Ga in  $h$ -BGaN alloys. Instead, the Ga composition in  $h$ -Ga $_x$ B $_{1-x}$ N alloys were determined by x-ray photoelectron spectroscopy (XPS) measurements. Figure 20.9(c) plots the dependence of  $x$  in  $h$ -Ga $_x$ B $_{1-x}$ N alloys on  $R_{\text{TMG}}$  utilizing the Ga compositions obtained

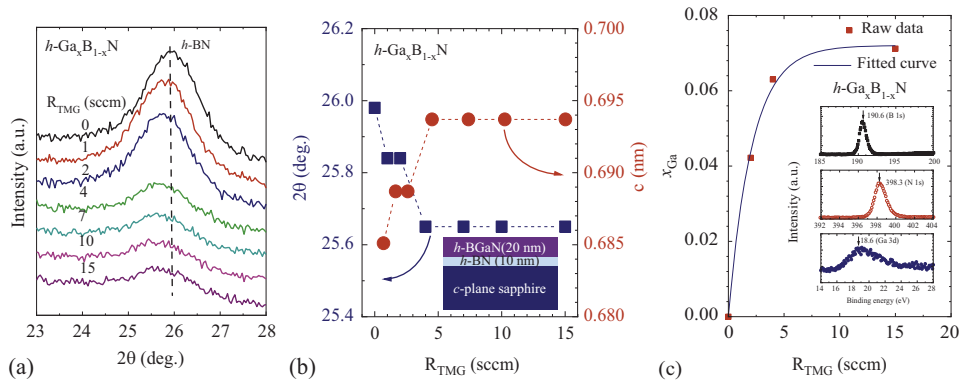


**Figure 20.9.** (a) The XRD (0002) diffraction peak intensity of  $h$ -BGaN alloys as a function of the  $R_{\text{TMG}}$ . (b) The XRD (0002) diffraction peak position (left axis) and the corresponding  $c$ -lattice constant (right axis) versus the TMGa flow rate,  $R_{\text{TMG}}$ . (c) The Ga composition ( $x$ ) in  $h$ -Ga $_x$ B $_{1-x}$ N alloys obtained via XPS measurements versus  $R_{\text{TMG}}$ . The solid curve is the least squares fit of data with equation (20.3). Inset: XPS spectra of an  $h$ -BGaN sample grown at  $R_{\text{TMG}} = 15$  sccm for B 1s, N 1s, and Ga 3d peaks, from which the alloy composition was determined (after [53]).

from XPS measurement data, which revealed that  $x$  in  $h\text{-Ga}_x\text{B}_{1-x}\text{N}$  sharply increases with  $R_{\text{TMG}}$  initially followed by a saturation with an onset occurring again at  $R_{\text{TMG}} \sim 4$  sccm; whereas  $x$  versus  $R_{\text{TMG}}$  can be described by the following equation [53]:

$$x = x_0[1 - \exp(-R_{\text{TMG}}/A)], \quad (20.3)$$

where  $x_0$  denotes the saturation value of Ga composition and  $A$  describes an exponential dependence of  $x$  in  $h\text{-Ga}_x\text{B}_{1-x}\text{N}$  with  $R_{\text{TMG}}$ . The least squares fit between the experimentally measured Ga compositions with equation (20.3) yielded a saturation value for the Ga composition of  $x_0 = (7.2 \pm 0.2)\%$  and  $A = 2.14 \pm 0.17$  sccm. The Ga composition saturation behavior shown in figure 20.9(c) is consistent with the observed onset behavior exhibited in the dependence of the XRD intensity and  $c$ -lattice constant on the TMGa flow rate shown in figure 20.9(b).

The observation of the onset point occurring at  $R_{\text{TMG}} = 4$  sccm suggests that only a limited fraction of GaN, up to  $\sim 7.2\%$ , can be incorporated into  $h\text{-BN}$  [53]. Since the temperature employed for the growth of  $h\text{-BGaN}$  alloys of  $1225^\circ\text{C}$  is higher than the decomposition temperature of GaN, it is plausible to attribute the Ga composition saturation to GaN decomposition at high growth temperature [53, 54]. However, the calculation results shown in figure 20.8(a) clearly revealed that the hexagonal structure can be stabilized in free-standing (BN)-rich BGaN alloys only for a B composition greater than 93% or equivalently for a Ga composition  $x \leq 7\%$  [75, 76]. In fact, the experimentally observed Ga saturation composition in  $h\text{-B}_{1-x}\text{Ga}_x\text{N}$  of  $x_0 \sim 7.2\%$  [53] is in perfect agreement with the theoretical prediction of the critical Ga composition of  $\sim 7\%$ , as illustrated in figure 20.8(a) [75, 76]. It is interesting to note that the theoretical prediction is made for free-standing  $h\text{-B}_{1-x}\text{Ga}_x\text{N}$  [75, 76], whereas the MOCVD grown layers were deposited on  $h\text{-BN}$  epilayer templates [53, 54]. Another interesting observation is that the theoretical calculation suggested that the use of AlN or GaN substrate promotes  $\text{B}_{1-x}\text{Ga}_x\text{N}$  alloys to crystallize into the ZB and WZ phase owing to the large cohesive energy of BN with the lattice constraint of the WZ-AlN or WZ-GaN substrate [75, 76]. This also explains the fact that experimentally the use of  $h\text{-BN}$  templates is necessary to promote the crystallization of  $h\text{-B}_{1-x}\text{Ga}_x\text{N}$  alloys into the hexagonal lattice [53, 54].

Since undoped  $h\text{-BN}$  is highly insulating and unintentionally doped GaN is usually conductive, one expects that the conductivity of the  $h\text{-B}_{1-x}\text{Ga}_x\text{N}$  alloy system increases with an increase in  $x$ . Indeed, the measured electrical resistivity values for  $h\text{-BGaN}$  were  $\rho \approx 5 \times 10^{10}$ ,  $5 \times 10^6$ , and  $2 \times 10^6 \Omega \cdot \text{cm}$  for  $x = 0$ , 0.045, and 0.07, respectively, corresponding to an enhancement in the electrical conductivity of four orders of magnitude as the Ga composition in  $h\text{-B}_{1-x}\text{Ga}_x\text{N}$  was increased from 0 to 0.07. This ability to control conductivity is expected to be very useful for certain device applications [53].

### 20.3.2 Growth of $h\text{-BGaN}$ QWs and photoluminescence emission properties

With the baseline for the growth of  $h\text{-BGaN}$  epilayers established, the growth of an  $h\text{-BN/Ga}_x\text{B}_{1-x}\text{N/BN}$  QW was attempted [53]. As for the growth of  $h\text{-BGaN}$

epilayers, prior to the deposition of a 2 nm thick  $h$ -BGaN QW, a 10 nm thick  $h$ -BN epilayer was first deposited on a  $c$ -plane sapphire substrate at 1300 °C to serve as a template as well as the bottom barrier layer. To avoid GaN decomposition in the well region, the growth temperature of the well and the top  $h$ -BN barrier was set to be the same as that of the  $h$ -BGaN epilayers at 1225 °C. A 2 nm thick  $h$ -BGaN epilayer without the top  $h$ -BN barrier was also grown as a reference for direct comparison. The targeted GaN fraction in the well region and in the reference  $h$ -BGaN epilayer was  $\sim 4\%$ . The layer structures of the  $h$ -BN/Ga $_x$ B $_{1-x}$ N/BN QW and the reference  $h$ -Ga $_x$ B $_{1-x}$ N epilayer are schematically shown in figure 20.10.

Figure 20.10 presents the low temperature photoluminescence spectra for the (a)  $h$ -BN/BGaN/BN QW and (b)  $h$ -BGaN reference epilayer. The dominant peaks around 4 eV are due to the recombination of a donor–acceptor pair and its phonon replicas involving the 200 meV longitudinal optical phonon mode [78–80], whereas the band-edge emission line near 5.55 eV in the  $h$ -BGaN alloy can be attributed to the recombination of bound excitons (or self-trapped excitons) [14, 78–81]. One of the distinctive features exhibited by the PL spectra of both the  $h$ -BN/BGaN/BN QW and  $h$ -BGaN reference epilayer is a pair of very sharp band-edge transition lines with an energy separation of exactly 170 meV (at 5.57 and 5.4 eV for  $h$ -BN/BGaN/BN QW and at 5.55 and 5.38 eV for the  $h$ -BGaN reference epilayer). This observed energy separation matches perfectly with the phonon energy of the  $E_{2g}$  symmetry vibration mode in  $h$ -BN ( $\Delta\sigma = 1371 \text{ cm}^{-1}$ ) [82]. The PL results thus suggest that the 5.38 eV (5.40 eV) emission line is the one-phonon replica of the 5.55 eV (5.57 eV) zero-phonon line. Since the  $E_{2g}$  symmetry vibration mode corresponds to the in-plane stretch of B and N atoms, the observation of a pronounced phonon replica line involving  $E_{2g}$  symmetry vibration mode corroborates the XRD results shown in

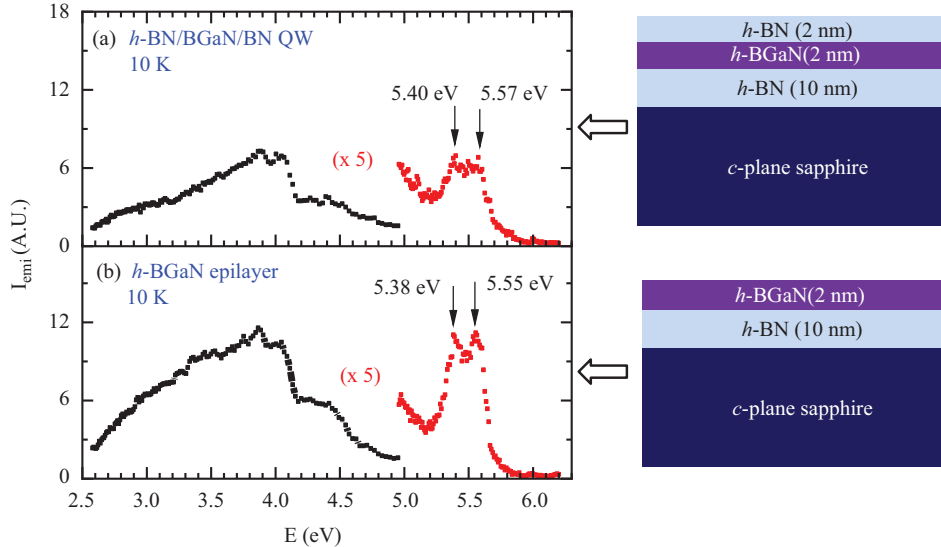


**Figure 20.10.** Low temperature (10 K) photoluminescence spectra for (a)  $h$ -BN/B $_{1-x}$ Ga $_x$ N/BN ( $x \sim 0.04$ ) QW and (b)  $h$ -B $_{1-x}$ Ga $_x$ N ( $x \sim 0.04$ ) epilayer. The layer structures are shown to the right. (After [53]).

figure 20.9(a) and further confirms that BN/BGaN/BN QW and BGaN epilayers have been crystallized into the hexagonal phase with a reasonable layered structure.

In comparison, the PL spectral line shapes of the 2 nm thick *h*-BGaN epilayer and 2 nm *h*-BGaN QW are quite similar. However, a careful inspection reveals that both the band-edge emission and its phonon replica lines in *h*-BGaN QW were slightly blue shifted by  $\sim 20$  meV with respect to those in the *h*-BGaN epilayer. This seems to suggest that a layer-structured QW has been successfully synthesized. Moreover, the results revealed that the formation of *h*-BN/BGaN/BN QW induces a quantum confinement effect, as in the conventional QWs. However, due to the larger exciton binding energy ( $\sim 0.7$  eV) [31–35] and smaller exciton Bohr radius ( $\sim 0.1$  nm) [34] in *h*-BN (and hence in B-rich *h*-BGaN), the confinement effect in *h*-BGaN QW is expected to be less visible in PL emission spectra than in more conventional QWs (e.g. GaN/AlN) with the same well width. However, *h*-BN barrier layers are necessary to facilitate carrier injection. These layer structures and the results shown in figures 20.9 and 20.10 provide a foundation for the further development of *h*-BGaN QW-based optoelectronic devices.

### 20.3.3 Probing the critical thickness and phase separation effects in *h*-GaBN/BN heterostructures

Despite the fact that the equilibrium phases of GaN and BN are wurtzite and hexagonal, respectively, the results described in the previous sub-sections demonstrated the successful synthesis of  $\text{Ga}_x\text{B}_{1-x}\text{N}$  alloys as well as *h*- $\text{Ga}_x\text{B}_{1-x}\text{N}$ /BN QWs in the hexagonal phase using MOCVD, with a maximum incorporation of Ga composition up to  $\sim 7.2\%$  at a growth temperature of 1225 °C [53]. This experimentally observed maximum Ga composition in *h*- $\text{Ga}_x\text{B}_{1-x}\text{N}$  agrees perfectly with the theoretical calculation results of  $\sim 7\%$  [75, 76]. The agreement between experimental and calculation results seems to suggest that GaN decomposition at relatively high growth temperatures is not a factor which limits the maximum Ga composition in *h*- $\text{Ga}_x\text{B}_{1-x}\text{N}$ , but rather it is the different equilibrium crystalline phases between BN (hexagonal) and GaN (wurtzite) which limits the incorporation of Ga in *h*- $\text{Ga}_x\text{B}_{1-x}\text{N}$ . It is desirable to find ways to produce *h*-GaBN alloys offering an extended range of variation in the bandgap as well as in the optical and electrical properties. However, this would require a better understanding of the basic properties of *h*- $\text{Ga}_x\text{B}_{1-x}\text{N}$ /*h*-BN heterostructures. One of the fundamental issues of heterostructure epitaxy is the critical thickness. Another correlated and critical issue is the evolution of the phase separation with the layer thickness.

Two sets of *h*-GaBN samples with varying *h*-GaBN thicknesses deposited on *h*-BN epi-templates grown under the TMG flow rates of  $R_{\text{TMG}} = 5$  and 20 sccm were synthesized for the investigation of the critical thickness ( $L_C$ ) phenomenon in the *h*-GaBN/BN heterostructure system [54]. The layer structure is identical to that shown in the inset of figure 20.9(b). Based on the results shown in figure 20.9(c), the TMG flow rates employed were beyond the onset point of  $R_{\text{TMG}} = 4$  sccm and hence the expected Ga contents in *h*-GaBN layers with varying thicknesses ( $d$ ) should be greater than  $x_0$  ( $\approx 0.072$ ). The microscopy images of a set of samples grown under

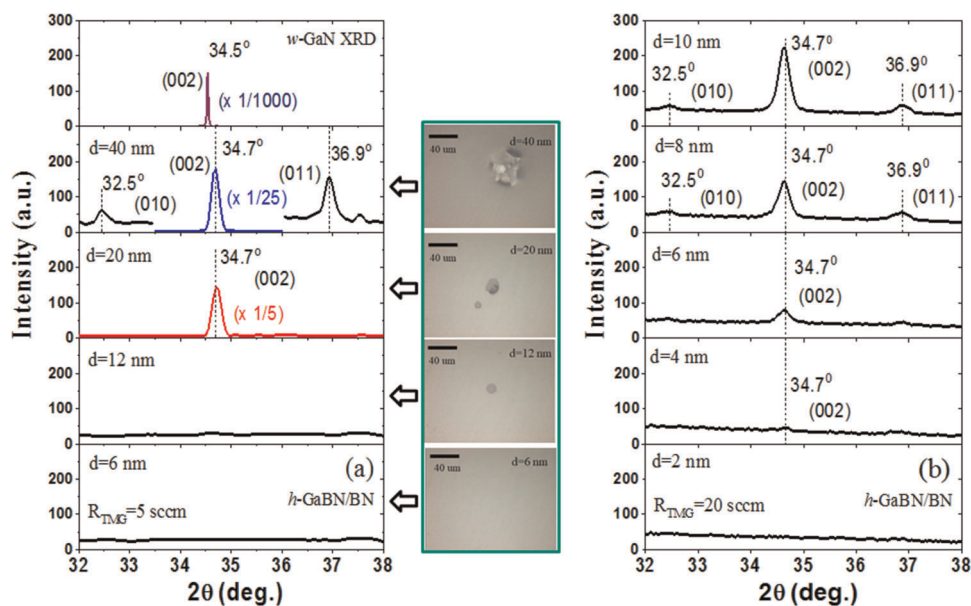


**Figure 20.11.** XRD  $\theta$ - $2\theta$  scans of *h*-GaN/BN heterostructure samples of different layer thickness grown under (a)  $R_{\text{TMG}} = 5$  sccm and (b)  $R_{\text{TMG}} = 20$  sccm. For reference, an XRD  $\theta$ - $2\theta$  scan of the (002) peak for a wurtzite-GaN (w-GaN) epilayer is shown in the top panel of in (a). The inset contains microscopy images of *h*-GaN alloy samples grown under  $R_{\text{TMG}} = 5$  sccm with different thicknesses (after [54]).

$R_{\text{TMG}} = 5$  sccm are shown in the inset of figure 20.11(a) and the results indicate that the 6 nm thick *h*-GaN layer sample exhibits a very smooth surface. However, the formation of extra complex features with sizes that increase with the layer thickness ( $d$ ) is clearly observed in films with thicknesses  $>12$  nm. For the film with  $d = 40$  nm, the size of the extra features becomes quite large with a diameter as large as  $50 \mu\text{m}$ . XRD  $\theta$ - $2\theta$  scans were employed to assess the crystalline structures of both sets of samples grown under (a)  $R_{\text{TMG}} = 5$  sccm and (b) 20 sccm with different thicknesses and the results are shown in figure 20.11, covering the spectral range of the wurtzite (w)-GaN (002) peak between  $32^\circ$  and  $38^\circ$ . An XRD  $\theta$ - $2\theta$  scan of an MOCVD grown wurtzite (w)-GaN epilayer is included for reference in the top panel of figure 20.11(a), which exhibits the expected w-GaN (002) peak at  $34.5^\circ$ . As shown in figure 20.11(a), for the set of samples grown with  $R_{\text{TMG}} = 5$  sccm, no w-GaN peak was observed for  $d = 6$  and 12 nm. However, the w-GaN (002) peak was clearly resolved at about at  $34.7^\circ$  in thick layers with  $d = 20$  nm and 40 nm. The shift in the (002) peak position from  $34.5^\circ$  for the w-GaN epilayer to  $34.7^\circ$  for the w-GaN domains inside *h*-GaN alloys is most likely due to the presence of strain in w-GaN domains. As the thickness ( $d$ ) further increases to 40 nm, in addition to the GaN (002) peak, other diffraction peaks corresponding to w-GaN (010) at  $32.5^\circ$  and GaN (011) at  $36.9^\circ$  were also observable. For the set of samples grown under  $R_{\text{TMG}} = 20$  sccm, the w-GaN (002) peak was absent only in the sample with  $d = 2$  nm and it starts to appear at  $d = 4$  nm, as shown in figure 20.11(b). The (010) peak

and (011) peak of the w-GaN phase were also observed as  $d$  further increases to above 6 nm. Compared with the XRD results of the reference w-GaN epilayer sample, the XRD results of  $h$ -GaBN alloys suggest that the extra features seen in figure 20.11 are related to the formation of the w-GaN phase inside the  $h$ -GaBN alloy matrix and they are only observable when the  $h$ -GaBN layer thickness is beyond 12 nm in samples grown under  $R_{\text{TMG}} = 5$  sccm (figure 20.11(a)) and 2 nm in samples grown under  $R_{\text{TMG}} = 20$  sccm (figure 20.11(b)).

Room temperature PL spectra for these two sets of  $h$ -GaBN/BN heterostructure samples have been measured and are plotted in figure 20.12 for samples grown under (a)  $R_{\text{TMG}} = 5$  sccm and (b)  $R_{\text{TMG}} = 20$  sccm. The PL spectrum of a standard w-GaN epilayer is also included in the top panel of figure 20.12(a) for reference, which exhibits a strong band-edge emission line in w-GaN at 3.39 eV. For films grown under  $R_{\text{TMG}} = 5$  sccm, the band-edge emission line from the wurtzite phase GaN is absent for the sample with a thickness of  $d = 6$  nm and a small peak near 3.34 eV starts to emerge for samples with  $d > 12$  nm. In fact, this emission line at 3.34 eV becomes rather prominent in the sample with  $d = 40$  nm. We believe that the new 3.34 eV line is the band-edge emission of w-GaN domains inside  $h$ -GaBN, which is redshifted with respect to 3.39 eV observed in w-GaN epilayers. It is reasonable to attribute the cause of this redshift in the PL emission peak in w-GaN domains with respect to that of the w-GaN epilayer to the same strain which produced a small shift

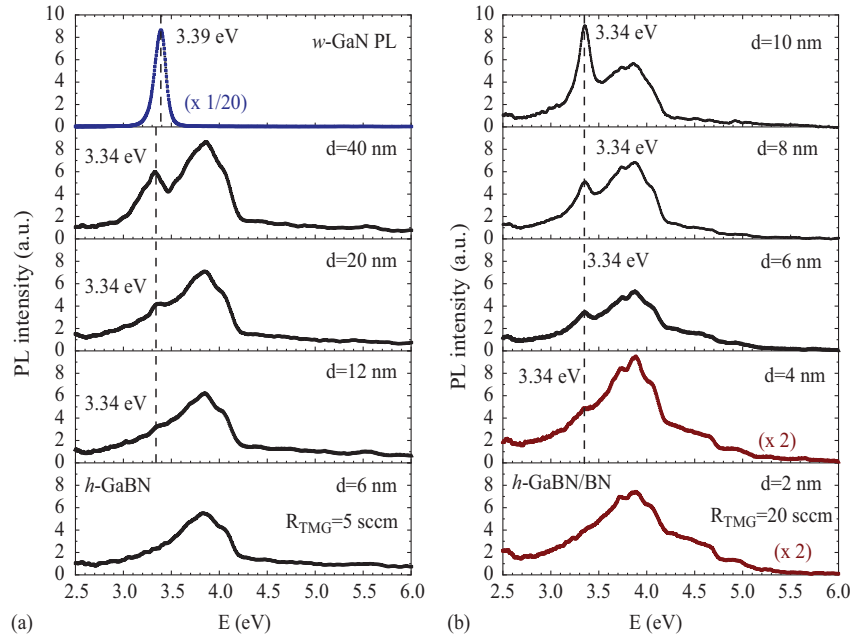


**Figure 20.12.** Room temperature photoluminescence spectra of  $h$ -GaBN/BN heterostructures of different layer thickness,  $d$ , for samples grown under (a)  $R_{\text{TMG}} = 5$  sccm and (b)  $R_{\text{TMG}} = 20$  sccm. For reference, the PL spectra of a wurtzite-GaN (w-GaN) epilayer is presented in the top panel of (a) (after [54]).

in the XRD (002) peak position of w-GaN domains in *h*-GaBN alloys with respect to that of w-GaN epilayer shown in figure 20.11.

For samples grown under  $R_{\text{TMG}} = 20$  sccm, the emission line near 3.34 eV related to w-GaN domains was absent only in the sample with  $d = 2$  nm and becomes the dominant emission line in the sample with  $d = 10$  nm. PL results for both sets of samples show that the emission line near 3.34 eV related to w-GaN domains increases with the *h*-GaBN thickness ( $d$ ) when  $d$  is beyond a critical thickness. Thus, the PL results collaborate the XRD results well. In addition to the band-edge emission line of w-GaN domains in *h*-GaBN observed at 3.34 eV, a broad peak near 3.9 eV is believed to be associated with a shallow donor to deep acceptor (DAP) transition in *h*-GaBN alloys, as its spectral features and peak position are very close to a DAP transition in the *h*-BN epilayers [80].

The XRD and PL results conclusively show that there exists a critical thickness below which  $\text{B}_x\text{Ga}_{1-x}\text{N}$  alloys of single hexagonal phase can be synthesized. One of the very surprising observations is the absence of the zinc blende (ZB) GaN domains inside the *h*-GaBN alloy matrix, despite the fact that the calculation results revealed that the ZB structure tends to be stabilized over a wide boron composition range for  $\text{B}_x\text{Ga}_{1-x}\text{N}$  alloys [75, 76]. Based on the calculation results, one expects a phase transition between hexagonal and zinc blende to occur when the layer thickness exceeds the critical thickness. However, the XRD and PL results shown in figures 20.11 and 20.12 clearly revealed that  $\text{B}_x\text{Ga}_{1-x}\text{N}$  alloy samples contain only W-GaN domains when their layer thicknesses exceed a critical thickness ( $L_C$ ).

To determine the critical thickness ( $L_C$ ) quantitatively, figure 20.13(a) plots the w-GaN (002) XRD peak intensity versus the layer thickness of *h*-GaBN alloys ( $d$ ) for (a)  $R_{\text{TMG}} = 5$  sccm and (b)  $R_{\text{TMG}} = 20$  sccm. The intensity of the w-GaN (002) peak at  $34.7^\circ$  displays a power law dependence on  $d$  when  $d$  is beyond  $\sim 6$  nm for  $R_{\text{TMG}} = 5$  sccm and  $\sim 2$  nm for  $R_{\text{TMG}} = 20$  sccm. We believe that the results are indicative of a phase separation, meaning that w-GaN domains start to form inside layer-structured *h*-GaBN alloys when  $d$  is beyond a critical layer thickness ( $L_C$ ). When the *h*-GaBN film thickness is less than  $L_C$ , no phase separation occurs. The relationship between the XRD w-GaN (002) peak intensity ( $I_{\text{XRD}}$ ) and *h*-GaBN layer thickness  $d$  can be described by

$$I_{\text{XRD}}(d) = I_0(d - L_C)^n. \quad (20.4)$$

The least squares fit of data with equation (20.4) yielded values of  $L_C = 6.0$  nm and 2.3 nm for the two sets of samples grown with  $R_{\text{TMG}} = 5$  sccm and 20 sccm, respectively, with the other fitting parameters being  $I_0 = 3.0$  (1.5),  $L_C = 6.0$  nm (2.3 nm), and  $n = 2.1$  (2.4) for  $R_{\text{TMG}} = 5$  sccm (20 sccm). The results shown in figure 20.13 indicate that the critical thickness,  $L_C$ , depends on the total Ga composition in *h*-GaBN alloys, as expected. The w-GaN (002) peak intensity increases with  $L_C$  following a power law dependence with an exponent  $n$  being very close to 2, which is probably related to the fact that *h*-GaBN films are 2D in nature. The results suggest that the formation of w-GaN polycrystalline structures inside *h*-GaBN occurs when  $d$  is larger than  $L_C$ .

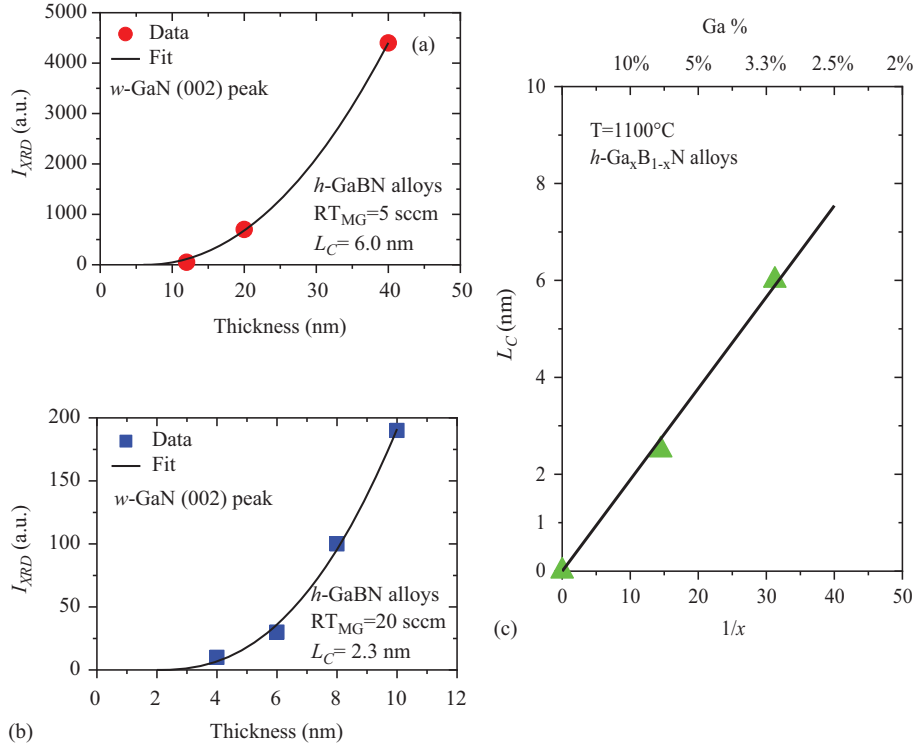


**Figure 20.13.** The wurtzite-GaN (w-GaN) (002) peak intensity versus  $h$ -GaBN alloy layer thickness for samples grown under (a)  $R_{TMG} = 5$  sccm and (b)  $R_{TMG} = 20$  sccm. The solid curves are the least squares fit of data with equation (20.4). (c) The Ga composition ( $x$ ) dependence of the critical thickness ( $L_C$ ) of  $h$ -Ga $_x$ B $_{1-x}$ N/BN heterostructures. The solid triangles show experimental data and the solid line is the least squares fit of data with equation (20.7) (after [54]).

Phase separation in ternary alloys  $A_xB_{1-x}C$  is generally due to the internal elastic strain, caused by the lattice constant mismatch between two binary constituents AC and BC and the underlying epilayer template [83, 84]. The origin of phase separation observed in  $h$ -GaBN alloys differs from a ternary alloy of the same crystalline structure such as InGaN alloys. The calculation results shown in figure 20.8 predicted a phase transition from hexagonal to zinc blende structure in GaBN alloys when the Ga composition is greater than 7%. However, the experimental results shown in figures 20.11 and 20.12 indicate that a phase separation between hexagonal and wurtzite structures occurs at a critical layer thickness ( $L_C$ ). Initially, the stable phase of BN in our growth condition is hexagonal, while that of GaN is wurtzite. This implies that a phase separation will occur when the Ga composition is above a critical value. Therefore, it is not a surprise to observe a phase separation in  $h$ -GaBN alloys. What is interesting, however, is the observation of the critical thickness in this layer-structured alloy system. It is well known that the interlayer interaction is very weak in 2D materials. However, the results shown in figures 20.11 and 20.12 indicate that interlayer interaction is strong enough to give rise to a critical

thickness in  $h$ -GaBN alloys, beyond which phase separation is to set in. The critical thickness ( $L_C$ ) of a lattice mismatched heterostructure can be calculated based on the strain energy [84, 85] and can be further simplified to the following relation [86]:

$$L_C(\text{nm}) \cong 0.1 \frac{a_s}{f}, \quad (20.5)$$

where  $a_s$  is the lattice constant of the underlying template ( $h$ -BN) and  $f$  is the misfit between the subsequent epilayer ( $h$ -Ga $_x$ B $_{1-x}$ N layer) and the underlying template layer, which is defined by

$$f = \frac{a_e - a_s}{a_s} = \frac{b}{a_s} x. \quad (20.6)$$

Here,  $a_e$  denotes the lattice constant of the  $h$ -Ga $_x$ B $_{1-x}$ N layer, which is proportional to the Ga composition,  $x$ . From equations (20.5) and (20.6) a simple linear relationship between the critical thickness  $L_C$  and Ga composition  $x$  in  $h$ -Ga $_x$ B $_{1-x}$ N alloys can be obtained as follows:

$$L_C(\text{nm}) = A \frac{1}{x}, \quad (20.7)$$

where  $A$  is a proportionality constant. The average Ga compositions in Ga $_x$ B $_{1-x}$ N alloys were determined by XPS measurements [54]. For instance, the measured average B, N, and Ga compositions in the sample with  $d = 10$  nm grown under  $R_{\text{TMG}} = 20$  sccm were 46.5%, 50.1%, and 3.4%, respectively, corresponding to a  $h$ -Ga $_x$ B $_{1-x}$ N alloy with  $x = 0.068$ . For the sample with  $d = 6.0$  nm grown under  $R_{\text{TMG}} = 5$  sccm, the average Ga composition in the  $h$ -Ga $_x$ B $_{1-x}$ N alloys deduced from the XPS measurements was  $x = 0.034$ . The experimentally measured  $L_C$  for these two samples with different Ga composition  $x$  are plotted in figure 20.13(c). Fitting of  $L_C$  versus  $1/x$  with equation (20.7) by including the point at the origin provides a fitting parameter  $A = 0.19$ . It is interesting to note that the simplified relationship of equation (20.7), which was developed for 3D materials, appears to adequately describe the critical thickness phenomenon in layered heterostructures.

Based on the theoretical calculation results shown in figure 20.8 [75, 76] and experimental results for thick (20 nm)  $h$ -Ga $_x$ B $_{1-x}$ N alloys shown in figure 20.9 [53], the expected maximum Ga composition in single phase hexagonal  $h$ -Ga $_x$ B $_{1-x}$ N alloys is about 7.2%. However, the results shown in figure 20.13(c) means that it is possible to increase the Ga composition in  $h$ -GaBN alloys without phase separation by further reducing the  $h$ -GaBN layer thickness. For instance, if we consider the extreme case of  $L_C = 1$  monolayer = 0.33 nm, the results shown in figure 20.13(c) imply that it is possible to synthesize  $h$ -Ga $_x$ B $_{1-x}$ N films with a Ga composition as high as  $x = 0.55$  without phase separation. These results therefore provide the first order baseline to guide the further development of layered  $h$ -GaBN/BN heterostructure and QWs.

## 20.4 Epitaxy growth and properties of $h$ -(BN)C semiconductor alloys

The  $h$ -BNC alloy system appears to possess the advantages of identical crystalline structure (hexagonal) and excellent matches in lattice constants (with an in-plane  $a$ -lattice constant mismatch of only about 1.5% between graphite and  $h$ -BN), thermal expansion coefficients, and melting points throughout the entire alloy range and potentially offers the possibility of synthesizing homogeneous  $h$ -BNC alloys in a wide range of compositions. However, it has been proven theoretically [87, 88] and experimentally [89–91] that synthesizing homogeneous  $h$ -BNC alloys is very challenging due to the strong inter-atomic bonds between B–N and C–C and the large difference in the bond energies, with respective bond energies of 4.0 eV (B–N) and 3.71 eV (C–C) compared with values of 2.83 eV for the C–N bond and 2.59 eV for the C–B bond [92, 93]. Consequently, atomic arrangements with C–C and B–N bonds are energetically favored over the ones with B–B and N–N bonds, leading to phase separation in  $h$ -BNC alloys [87, 88]. In general, the expression of  $(\text{BN})_{1-x}(\text{C}_2)_x$  for these alloys is used because C atoms tend to incorporate as C–C ( $\text{C}_2$ ) pairs [92]. Atomic layers consisting of hybridized, randomly distributed domains of  $h$ -BN and C phases with compositions ranging from pure BN to pure graphene have been synthesized by various growth techniques [89–91], making the distributions of atoms in these alloy materials far from perfectly random.

Phase stability for a monolayer  $h$ -BNC alloy system was examined using Monte Carlo simulations and the cluster expansion technique based on first-principles calculations to serve as a foundation for understanding the phase stability of  $h$ - $(\text{BN})_x(\text{C}_2)_{1-x}$  alloys [87]. The simulation results revealed several key finds [87]: (i) no stable intermediate phase exists between monolayer BN and graphene through construction of a ground-state diagram—the formation energies for all the possible atomic arrangements are positive; (ii) the atomic arrangements strongly favor neighboring B–N and C–C bonds and disfavor B–C and C–N atoms; (iii) no B–B and N–N atoms exist for these atomic arrangements; (iv) complete miscibility requires a very high growth temperature and the critical temperature for complete miscibility is around  $T_c = 4500$  K; (v) random alloys can only exist for extremely small carbon or BN compositions; and (vi) lattice vibration enhances the solubility limits in (BN)-rich and C-rich  $h$ - $(\text{BN})_x(\text{C}_2)_{1-x}$  alloys and also reduces the critical temperature of complete miscibility from  $T_c = 4500$  K to  $T_c = 3500$  K.

As with any new semiconductor material in the development stage, the ability to synthesize large wafers of homogenous alloys (instead of domains) is essential for the realization of technologically significant device applications. There was, however, experimental evidence for obtaining homogeneous  $h$ - $(\text{BN})_x(\text{C}_2)_{1-x}$  alloys with  $x = 0.5$  ( $\text{BNC}_2$ ) [93, 94]. These  $\text{BC}_2\text{N}$  thin films were prepared using CVD with acetonitrile and boron trichloride and helium gas as a carrier gas to ensure forward flow of the reactants and deposited thin films on the cleaved surfaces of  $h$ -BN substrates at a substrate temperature of about  $\sim 850$  °C [94]. The bandgap was examined using scanning tunneling microscopy (STM) and PL emission spectroscopy and the results are shown in figure 20.14. The results of the current–voltage ( $I$ – $V$ ) using STM measurements are shown in figure 20.14(a). The differential

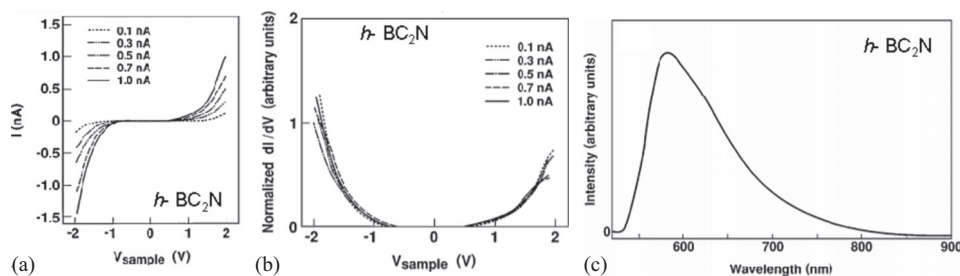


**Figure 20.14.** (a) Spectroscopic data obtained using STM for the cleaved surface of an  $h\text{-(BN)}_{1-x}\text{(C}_2\text{)}_x$  alloy sample with  $x = 0.5$  ( $\text{BC}_2\text{N}$ ) and an Re tip. Each curve is acquired at constant tip-sample separation, which was controlled by tunneling currents of 0.1, 0.3, 0.5, 0.7, and 1.0 nA with a sample voltage of 2 V. (b) Normalized differential conductivity against sample bias voltage. (c) Photoluminescence spectrum taken from  $\text{BC}_2\text{N}$  thin film at a low temperature (4.2 K). Reproduced with permission from [94]. Copyright 1996 the American Physical Society.

conductivity,  $dI/dV$  shown in figure 20.14(b), deduced from the  $I$ - $V$  characteristics provides a measurement of the surface density of states. A  $dI/dV$  above 0 V corresponds to the conduction band and that below 0 V corresponds to the valence band. From figure 20.14(b), the bandgap of  $h\text{-BC}_2\text{N}$  thin films was estimated to be about 2 eV [94]. A typical low temperature (4.2 K) PL spectrum of these  $h\text{-BC}_2\text{N}$  thin films is shown in figure 20.14(c). The PL emission spectra exhibit peak energies at 600 nm at room temperature and 580 nm at 4.2 K, corresponding to 2.07 and 2.14 eV, respectively. These values agree well with the bandgap energy of 2 eV estimated using STM [94]. The observation of the PL emission peak corresponding well to the measured bandgap implies that that  $\text{BNC}_2$  is a direct bandgap semiconductor with an estimated bandgap energy  $E_g = 2.0$  eV [94].

More recently, thin films of homogeneous  $h\text{-(BN)}_{1-x}\text{(C}_2\text{)}_x$  alloys in both the BN-rich and C-rich sides have been synthesized using MOCVD by utilizing  $h\text{-BN}$  as a template [58–61]. Experimental results suggest that the critical carbon concentration ( $x_c$ ) to form the homogeneous  $h\text{-(BN)}_{1-x}\text{(C}_2\text{)}_x$  alloys in the BN-rich is about 3.2% and on the C-rich side is ~95% at a growth temperature of 1300 °C [58–60]. Furthermore, an enhancement of approximately 15 orders of magnitude in the electrical conductivity has been attained by increasing the carbon concentration ( $x$ ) from 0 ( $h\text{-BN}$ ) to 1 (graphite) [58–61]. These recent results are summarized in the sub-sections below.

#### 20.4.1 BN-rich $h\text{-(BN)}_{1-x}\text{(C}_2\text{)}_x$ alloys

Epitaxial layers of  $h\text{-(BN)}_{1-x}\text{(C}_2\text{)}_x$  alloys of about 60 nm in thickness were synthesized on sapphire (0001) substrates at 1300 °C using MOCVD. Prior to the growth of  $h\text{-(BN)}_{1-x}\text{(C}_2\text{)}_x$  alloy, a 5 nm thick  $h\text{-BN}$  epilayer was first deposited on sapphire to serve as a template for the subsequent growth of the  $h\text{-(BN)}_{1-x}\text{(C}_2\text{)}_x$  alloy. Triethylboron (TEB), ammonia ( $\text{NH}_3$ ), and propane ( $\text{C}_3\text{H}_8$ ) were used as the B, N, and C precursors, respectively, and hydrogen was used as a carrier gas. The carbon concentration was controlled by the  $\text{C}_3\text{H}_8$  flow rates [58]. A pulsed MOCVD

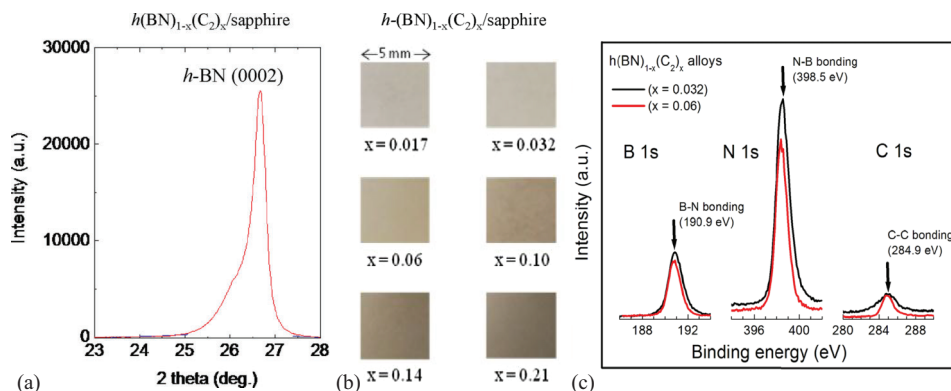


**Figure 20.15.** (a) An XRD  $\theta$ - $2\theta$  scan around the  $h\text{-BN (0002)}$  diffraction peak of an  $h\text{-BN}$  epilayer deposited on sapphire substrate. (b) Optical micrographs ( $5\text{ mm} \times 5\text{ mm}$ ) of a set of  $h\text{-BN}$ -rich  $h\text{-(BN)}_{1-x}(\text{C}_2)_x$  epilayers with different C concentrations deposited on sapphire substrate at the same temperature as the  $h\text{-BN}$  epilayer in (a). (c) XPS spectra of the B 1s, N 1s, and C 1s core levels for the  $h\text{-(BN)}_{1-x}(\text{C}_2)_x$  epilayers with  $x = 0.032$  and 0.06. Reproduced with permission from [58]. Copyright 2014 AIP Publishing.

epitaxial growth process was employed to grow the  $h\text{-(BN)}_{1-x}(\text{C}_2)_x$  alloys [61]. Both TEB and  $\text{C}_3\text{H}_8$  were transported together into the reactor and  $\text{NH}_3$  was supplied separately with respective flow rates of 0.06 sccm and 3.0 standard liters per minute (SLM). Samples were grown under N-rich conditions, ensuring a very high V-III ratio.  $\text{C}_3\text{H}_8$  flow rates were increased in small steps to obtain  $h\text{-(BN)}_{1-x}(\text{C}_2)_x$  alloys with different carbon concentrations ( $x$ ). The XRD  $\theta$ - $2\theta$  scan patterns of  $h\text{-(BN)}_{1-x}(\text{C}_2)_x$  samples have a similar spectral shape as those of the  $h\text{-BN}$  templates shown in figure 20.15(a). Figure 20.15(b) shows optical micrographs of a  $5\text{ mm} \times 5\text{ mm}$  area of  $h\text{-(BN)}_{1-x}(\text{C}_2)_x$  epilayers with different carbon concentrations. XPS measurements were employed to determine the carbon concentrations. Figure 20.15(c) shows the XPS spectra of B 1s, N 1s, and C 1s core levels for two representative  $h\text{-(BN)}_{1-x}(\text{C}_2)_x$  alloy samples with  $x = 0.032$  and  $x = 0.06$  [58]. Based on the bandgap value of  $h\text{-BN}$  ( $\sim 6\text{ eV}$ ) and the small values of  $x$  ( $x = 0$  to 0.21), these  $h\text{-(BN)}_{1-x}(\text{C}_2)_x$  epilayers should be transparent in the visible spectral range. However, only samples with  $x = 0, 0.017$ , and 0.032 are transparent. Samples with  $x = 0.06, 0.10, 0.14$ , and 0.21 appear dark and the darkness increases with an increase of  $x$ . We believe that this is due to the formation of C clusters in these alloys. The results shown in figure 20.15(b) seem to suggest that the critical C concentration,  $x_c$ , for homogeneous alloy formation or the solid solubility limit of C in  $h\text{-BN}$  is around 0.032 at a growth temperature of  $1300\text{ }^\circ\text{C}$ .

UV-visible optical absorption spectroscopy was employed to measure the bandgap variation with C incorporation. We have observed that the optical absorption edge of  $h\text{-(BN)}_{1-x}(\text{C}_2)_x$  epilayers decreases with an increase of the C concentration, as expected. The absorption coefficients ( $\alpha$ ) were obtained from the absorption spectrum. The energy bandgap  $E_g$  values were estimated from the Tauc plot of the absorption coefficients [95]. Figure 20.16(a) plots  $\alpha^2$  as a function of the excitation photon energy for  $h\text{-(BN)}_{1-x}(\text{C}_2)_x$  epilayers with  $x = 0.0, 0.017, 0.032, 0.06, 0.10, 0.14$ , and 0.21.  $E_g$  values were obtained from the intersections between

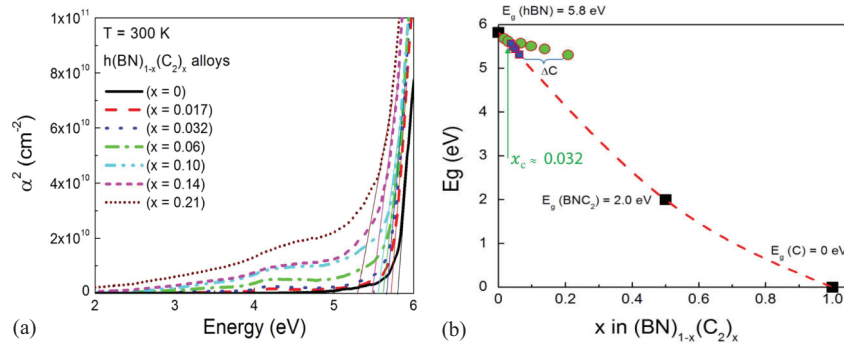


**Figure 20.16.** (a) Tauc plots of absorption coefficients of  $h$ -BN-rich  $h$ -(BN) $_{1-x}$ (C $_2$ ) $_x$  epilayers with different C compositions. (b) Energy bandgap  $E_g$  versus C composition in  $h$ -(BN) $_{1-x}$ (C $_2$ ) $_x$  alloys. Green circles are the measured data of  $E_g$  obtained from the optical absorption spectra shown in (a) and the total C concentrations from XPS. The dashed curve is the plot of equation (20.8),  $E_g[h$ -(BN) $_{1-x}$ (C $_2$ ) $_x] = (1 - x)E_g(h$ -BN) +  $x E_g(C) - b(1 - x)x$ , where  $E_g$  (graphite) = 0 eV and  $E_g$  (BNC $_2$ ) = 2.0 eV [94] were used, providing a fitted value of  $b = 3.6$  eV. Blue squares are the data points extrapolated from equation (20.8) representing the C concentrations in the homogeneous  $h$ -(BN) $_{1-x}$ (C $_2$ ) $_x$  alloys ( $y$ ), which is lower than the total C concentration in the samples ( $x$ ).  $\Delta C (= x - y)$  denotes the amount of excess C concentration in  $h$ -(BN) $_{1-x}$ (C $_2$ ) $_x$  alloys with  $x > x_c$  ( $\approx 0.032$ ) which ends up in the separated C phase. Reproduced with permission from [58]. Copyright 2014 AIP Publishing.

the straight lines and the horizontal axis to be 5.80, 5.70, 5.65, 5.60, 5.55, 5.47, and 5.30 eV for samples with  $x = 0.0, 0.017, 0.032, 0.06, 0.10, 0.14,$  and  $0.21$ , respectively. The optical absorption edge appears to be strongly affected by the excitonic effects because the actual bandgap of  $h$ -BN is near 6.4 eV. Figure 20.16(b) plots the measured excitonic bandgap  $E_g$  versus  $x$  for  $h$ -(BN) $_{1-x}$ (C $_2$ ) $_x$  epilayers that include the bandgap energies of  $h$ -BN ( $x = 0$ ), graphite, and  $h$ (BNC $_2$ ) from figure 20.14 [94]. The dashed curve represents a fitting using the general equation for describing the bandgaps of semiconductor ternary alloys,

$$E_g[h$$
-(BN) $_{1-x}$ (C $_2$ ) $_x] = (1 - x)E_g(h$ -BN) +  $x E_g(C) - b(1 - x)x, \quad (20.8)$

where  $x$  is the C composition in the  $h$ -(BN) $_{1-x}$ (C $_2$ ) $_x$  alloys and  $b$  is the bowing parameter.  $E_g(C) = 0$  is the energy bandgap of graphite. The fitted bowing parameter is  $b = 3.6$  eV. The green filled circles are the measured C concentrations obtained from XPS and the corresponding  $E_g$  values obtained from the optical absorption spectra. The results show that the data for samples with  $x = 0.017$  and  $0.032$  fit well with equation (20.8), suggesting the formation of homogeneous alloys.

Samples with  $x = 0.06, 0.10, 0.14,$  and  $0.21$  deviate significantly from equation (20.8). This is a result phase separation occurring in samples with  $x > x_c$  ( $\approx 0.032$ ). In the phase separated materials, the XPS measures the total carbon concentrations, while the carbon concentration deduced from the bandgap variation of equation (20.8) represents the carbon concentration in the homogeneous  $h$ -(BN) $_{1-x}$ (C $_2$ ) $_x$  alloy phase. Therefore, the deviation from equation (20.8) is a measure of the excess C concentration in the phase separated C clusters (graphite phase). In other words,

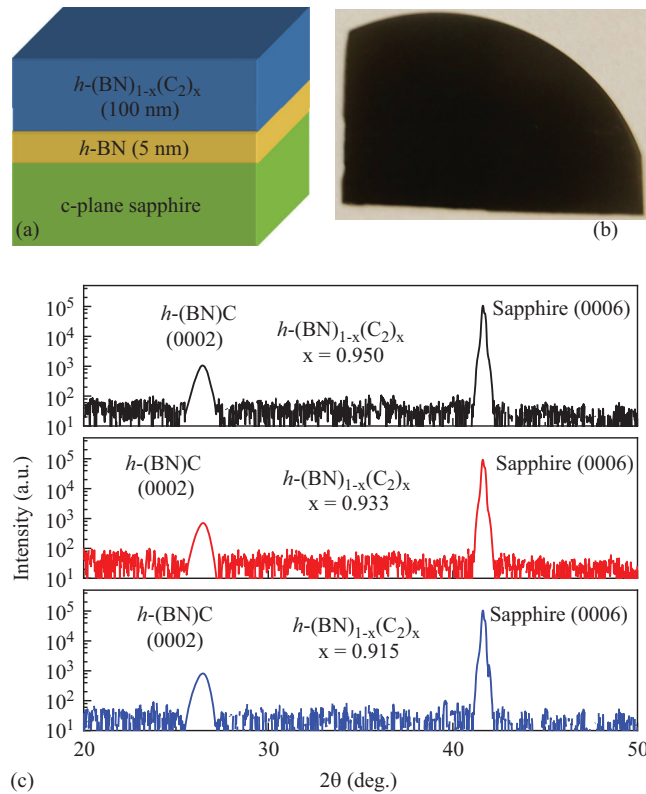


**Figure 20.17.** (a) Schematic of c-rich  $h\text{-(BN)}_{1-x}(\text{C}_2)_x$  epilayers. (b) Optical micrograph of a  $h\text{-(BN)}_{1-x}(\text{C}_2)_x$  alloy sample with  $x = 0.95$ . (c) XRD  $\theta$ - $2\theta$  scans of C-rich  $h\text{-(BN)}_{1-x}(\text{C}_2)_x$  epilayers grown on c-plane sapphire substrates under 1, 2, and 3 sccm  $\text{NH}_3$  flow rates (after [59]).

$h\text{-(BN)}_{1-x}(\text{C}_2)_x$  alloys with  $x > x_c$  ( $\approx 0.032$ ) contain separated carbon domain. The actual carbon concentrations ( $y$ ) in the homogeneous alloys is less than the total carbon concentration determined using XPS ( $x$ ). The carbon (C) concentrations in the homogeneous alloy phase ( $y$ ) are plotted as blue filled squares in figure 20.16(b), which are deduced from  $E_g$  measured by the optical absorption spectroscopy coupled with the use of equation (20.8). The C concentration difference between  $x$  and  $y$  is denoted as  $\Delta C = x - y$  (indicated in figure 20.16 (b)), which measures the excess carbon concentrations in the separated carbon phases (or graphite phase) in samples with  $x = 0.06, 0.10, 0.14,$  and  $0.21$ . However, at  $x > x_c$  the phases of  $h\text{-BN}$ , graphite, and  $h\text{-(BN)}_{1-y}(\text{C}_2)_y$  alloys with  $y < x$  co-exist.

#### 20.4.2 C-rich $h\text{-(BN)}_{1-x}(\text{C}_2)_x$ alloys

Epitaxial layers of  $h\text{-(BN)}_{1-x}(\text{C}_2)_x$  alloys ( $x \sim 0.92$  to  $0.95$ ) of about 100 nm in thickness, shown schematically in figure 20.17(a), were also synthesized on  $h\text{-BN}/c\text{-plane sapphire}$  templates [59, 61]. Triethylboron (TEB), ammonia ( $\text{NH}_3$ ), and propane ( $\text{C}_3\text{H}_8$ ) were used as the B, N, and C precursors, respectively. Samples

were grown using nitrogen as a carrier gas at 1300 °C. The carbon compositions were controlled during MOCVD by varying the  $\text{NH}_3$  flow rate and verified by XPS measurements, which revealed that  $x$  (the C mole fraction) decreases almost linearly with an increase in the  $\text{NH}_3$  flow rate (scm). This is due to the increase in BN fraction in the  $h\text{-(BN)}_{1-x}\text{(C}_2\text{)}_x$  epilayers with an increase in N ( $\text{NH}_3$  flow rate). Figure 20.17(b) shows the optical micrograph of an  $h\text{-(BN)}_{1-x}\text{(C}_2\text{)}_x$  alloy sample with  $x = 0.95$ . Based on the bandgap value of graphite (zero gap),  $h\text{-(BN)}_{1-x}\text{(C}_2\text{)}_x$  epilayers with large values of  $x$  should appear black under the visible light. Figure 20.17(c) shows XRD  $\theta$ - $2\theta$  scans of  $h\text{-(BN)}_{1-x}\text{(C}_2\text{)}_x$  samples with  $x \sim 95.0\%$ ,  $93.3\%$ , and  $91.5\%$ , revealing a lattice constant of  $c = 6.73 \text{ \AA}$  for all samples, which closely matches a value of  $c = 6.70 \text{ \AA}$  for graphite [96]. No other diffraction peaks were observed, which confirms the hexagonal crystalline structure of the  $(\text{BN})_{1-x}\text{(C}_2\text{)}_x$  epilayers grown using MOCVD. The slight increase in the  $c$  lattice constant over graphite is due to the fact that these films were grown on a  $h\text{-BN}$  template and experience a ‘compressive’-like strain in the  $c$ -plane.

Raman spectroscopy measurements were employed to probe the phase separation effect in C-rich  $h\text{-(BN)}_{1-x}\text{(C}_2\text{)}_x$  alloys. Raman spectra of pure  $h\text{-BN}$ , graphite, and selected  $h\text{-(BN)C}$  samples are shown in figure 20.18(a). The graphite spectrum exhibits the typical characteristic graphitic  $E_{2g}$ (G) vibration peak at  $1588 \text{ cm}^{-1}$  and the defect induced D peak at  $1345 \text{ cm}^{-1}$  [97]. The spectra of the  $h\text{-(BN)}_{1-x}\text{(C}_2\text{)}_x$  epilayers with  $x < 0.95$  show that the G peak and the D peak are at the same positions as those in graphite. This implies that the compositions in these  $h\text{-(BN)C}$  epilayers are phase separated with separate C–C domains. Moreover, the intensity and peak line widths of the  $E_{2g}$  modes of these samples are also like those of graphite. In contrast, the Raman spectrum of the  $h\text{-(BN)}_{1-x}\text{(C}_2\text{)}_x$  alloy with  $x = 0.95$  (black solid line) shows that the G peak shifted to  $1576 \text{ cm}^{-1}$  towards the

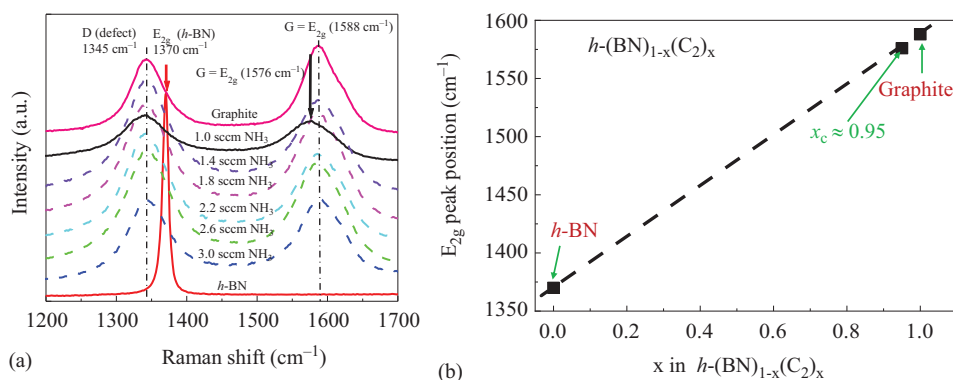


**Figure 20.18.** (a) Raman spectra of  $h\text{-BN}$  ( $x = 0$ ), graphite ( $x = 1$ ), and selected C-rich  $h\text{-(BN)}_{1-x}\text{(C}_2\text{)}_x$  epilayers grown at different  $\text{NH}_3$  flow rates. The G peak at  $1576 \text{ cm}^{-1}$  of the  $h\text{-(BN)}_{1-x}\text{(C}_2\text{)}_x$  alloy with  $x = 0.95$  (1 scm  $\text{NH}_3$  flow rate) shifts towards the  $\text{sp}^2$  bonded  $h\text{-BN}$  vibrational peak ( $1370 \text{ cm}^{-1}$ ), which is a signature of the formation of homogeneous  $h\text{-(BN)C}$  alloy. (b)  $E_{2g}$  vibration peak position versus  $x$  in C-rich  $h\text{-(BN)}_{1-x}\text{(C}_2\text{)}_x$  showing peak positions for  $h\text{-BN}$ , graphite, and  $h\text{-(BN)}_{1-x}\text{(C}_2\text{)}_x$  alloy with  $x = 0.95$ . The dashed line is a guide for the eyes (after [59]).

characteristic of a pure *h*-BN peak ( $1370\text{ cm}^{-1}$ ). Figure 20.18(b) plots the measured  $E_{2g}$  peak position versus  $x$  in  $h\text{-(BN)}_{1-x}\text{(C}_2\text{)}_x$  alloys using the measured values of *h*-BN, graphite, and  $h\text{-(BN)}_{1-x}\text{(C}_2\text{)}_x$  ( $x = 0.95$ ). Typically, the formation of homogeneous alloys leads to a shift in the Raman spectral peak that varies linearly according to the peak positions of the constituent atoms or binary compounds [98]. For homogeneous C-rich  $h\text{-(BN)}_{1-x}\text{(C}_2\text{)}_x$  alloys, the Raman peak position is expected to shift towards lower frequency with a decrease of  $x$ . The observed Raman peak shift for  $h\text{-(BN)}_{1-x}\text{(C}_2\text{)}_x$  alloy with  $x = 0.95$  suggests that homogeneous C-rich  $h\text{-(BN)}_{1-x}\text{(C}_2\text{)}_x$  alloys with  $x \geq 0.95$  have been successfully synthesized.

It is interesting to note that a slight deviation from the ideal (1:1) stoichiometry ratio between B and N could have a strong influence on the conductivity type of C-rich  $h\text{-(BN)}_{1-x}\text{(C}_2\text{)}_x$  [59]. This is because  $h\text{-(BN)}_{1-x}\text{(C}_2\text{)}_x$  alloys are formed by incorporating group-III (B) and group-V (N) atoms into the group-IV (C) lattice, in which B and N may also serve as dopants. N could replace C to give rise to n-type conductivity and B could replace C to give rise to p-type conductivity. Figure 20.19(a) shows the room temperature Hall-mobility and carrier concentration of *h*-(BN)C epilayers as functions of the  $\text{NH}_3$  flow rate employed during the MOCVD growth, which clearly revealed that the carrier type is p-type for samples synthesized under  $\text{NH}_3$  flow rates below 2.1 sccm and is n-type for the samples synthesized under  $\text{NH}_3$  flow rates above 2.1 sccm. The results thus indicate that when *h*-(BN)C alloys are synthesized under  $\text{NH}_3$  flow rates below 2.1 sccm, there are fewer N atoms than B atoms in the materials, leading to a p-type conductivity. Supplying more N atoms to the reaction zone by increasing the  $\text{NH}_3$  flow rate to above 2.1 sccm produces n-type materials because there are more N atoms than B atoms. This speculation is further verified by the XPS measurement results which revealed that samples synthesized under 1 and 2 sccm  $\text{NH}_3$  flow rates have a lower N concentration than B, while the sample synthesized under a 3 sccm  $\text{NH}_3$  flow rate has a higher N concentration than B [59, 61]. At  $\text{NH}_3 = 2.1$  sccm, C-rich  $h\text{-(BN)}_{1-x}\text{(C}_2\text{)}_x$  alloys have a 1:1 stoichiometry ratio between B atoms and N atoms,  $[\text{B}] = [\text{N}]$ , a transition from p- to n-type conductivity occurs [59, 61].

The measured background carrier concentrations at room temperature for both p- and n-type C-rich  $h\text{-(BN)}_{1-x}\text{(C}_2\text{)}_x$  epilayers are relatively high ( $\sim 1.5 \times 10^{20}\text{ cm}^{-3}$ ) [59]. This is mostly due to the fact that the energy bandgaps of C-rich *h*-(BN)C alloys are small and the energy level of the N donors (B acceptors) in C-rich *h*-(BN)C alloys is expected to be very shallow or possibly even lie within the conduction (valence band). The measured electron and hole mobilities ( $\mu_e$  or  $\mu_h$ ) and concentrations ( $n$  or  $p$ ) are quite comparable and their dependence on the  $\text{NH}_3$  flow rate are almost symmetric around  $\text{NH}_3 = 2.1$  sccm. The results suggest that the effective masses of electrons and holes in C-rich  $h\text{-(BN)}_{1-x}\text{(C}_2\text{)}_x$  alloys must be comparable, similar to the case of single sheet *h*-BN [34, 99]. In these alloys, the carrier mobility depends only on the carrier concentration near room temperature, whereas the room temperature mobility for both p- and n-type  $h\text{-(BN)}_{1-x}\text{(C}_2\text{)}_x$  epilayers is  $\sim 15\text{ cm}^2\text{ V}^{-1}\text{ s}^{-1}$ .

With the expectation of small bandgaps for C-rich  $h\text{-(BN)}_{1-x}\text{(C}_2\text{)}_x$  alloys, variable temperature van der Pauw Hall-effect measurements were attempted to extract the

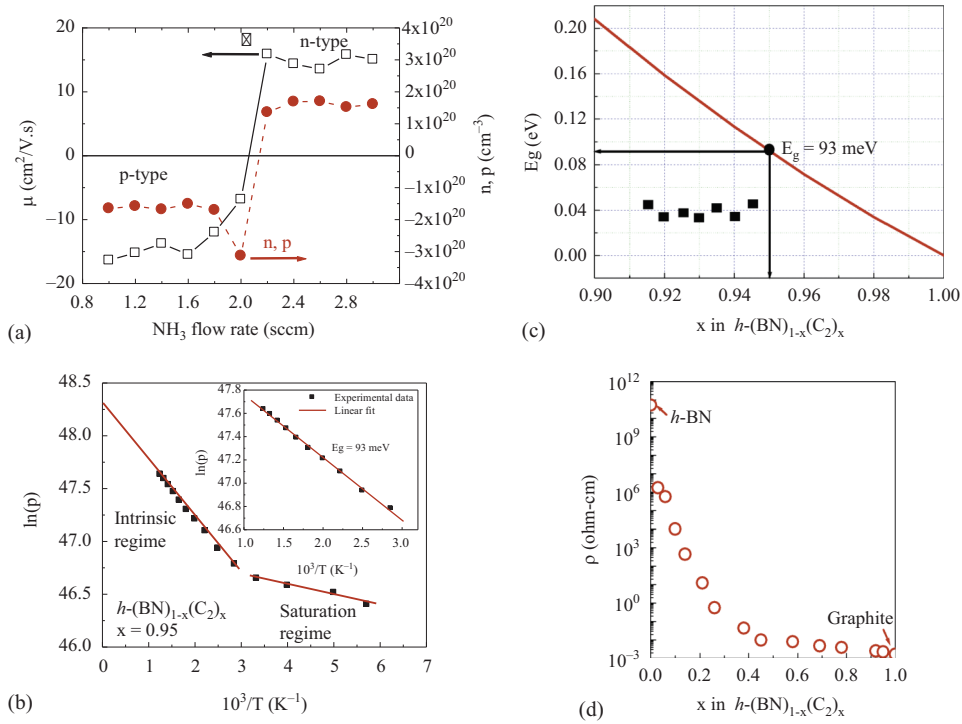


**Figure 20.19.** (a) Mobility and carrier concentration of C-rich  $h\text{-(BN)}_{1-x}(\text{C}_2)_x$  epilayers grown under different NH<sub>3</sub> flow rates. The carrier type in the alloys is p-type for NH<sub>3</sub> flow rates below 2.1 sccm and changes to n-type for NH<sub>3</sub> flow rates above 2.1 sccm. (b) Temperature dependent hole concentration plotted in the scale of  $\ln(p)$  versus  $1/T$  for an  $h\text{-(BN)}_{1-x}(\text{C}_2)_x$  sample with  $x = 0.95$ . The temperature dependence of the free carrier concentration shows a typical behavior of narrow gap semiconductors consisting of both saturation and intrinsic carrier conduction regime. The inset shows  $\ln(p)$  versus  $1/T$  plot for the intrinsic region, from which a bandgap  $E_g \sim 93$  meV is obtained. (c) Plot of the bandgap energy of  $h\text{-(BN)}_{1-x}(\text{C}_2)_x$  alloys versus carbon concentration ( $x$ ) in the C-rich side obtained from equation (20.8) with  $E_g(h\text{-BN}) = 6.4$  eV,  $E_g(\text{C}) = 0$  eV, and the bowing parameter of  $b = 4.8$  eV. The activation energy (or the bandgap) value of  $h\text{-(BN)}_{1-x}(\text{C}_2)_x$  with  $x = 0.95$  is marked as a solid circle on the plot of the bandgap variation of  $h\text{-(BN)}_{1-x}(\text{C}_2)_x$  with  $x$ . Activation energies of  $h\text{-(BN)}_{1-x}(\text{C}_2)_x$  epilayers with  $x < 0.95$  are also shown as solid squares, which deviate from the plot of the bandgap variation of  $h\text{-(BN)}_{1-x}(\text{C}_2)_x$  with  $x$ . (d) Room temperature resistivity (conductivity) of the  $h\text{-(BN)}_{1-x}(\text{C}_2)_x$  epilayers with different C concentrations, including  $h\text{-BN}$  and graphite (after [58] and [59]).

bandgap from the intrinsic carrier conduction regime [59]. Figure 20.19(b) shows the temperature dependence of the free hole concentration ( $p$ ) for the  $h\text{-(BN)}_{1-x}(\text{C}_2)_x$  sample with  $x = 0.95$  in the temperature range of 175–800 K. The dependence of the carrier concentration on temperature follows that of a very typical narrow bandgap semiconductor with two distinct regimes [100]. In the medium or low temperature region, nearly all acceptors are ionized, and the carrier concentration is nearly saturated and is independent of the temperature. In the high temperature region, the carrier concentration is predominantly intrinsic. The crossover from the saturation to the intrinsic conduction regime occurs around 350 K. The inset of figure 20.19(b) shows the Arrhenius plot of the carrier concentration in the intrinsic conduction

regime, in which the hole concentration ( $p$ ) and energy gap ( $E_g$ ) can be expressed in terms of temperature as

$$p \propto \exp\left(-\frac{E_g}{2k_b T}\right), \quad (20.9)$$

where  $k_b$  is the Boltzmann constant. The fitted value of  $E_g$  obtained for the  $h\text{-(BN)}_{1-x}\text{(C}_2)_x$  alloy ( $x = 0.95$ ) is  $\sim 93$  meV.

The bandgap value of  $\sim 93$  meV obtained from the temperature dependent carrier concentration in the intrinsic conduction region shown in figure 20.19(b) can be further verified by comparing it with the expected value. The expected bandgap variation of homogeneous  $h\text{-(BN)}_{1-x}\text{(C}_2)_x$  alloys with  $x$  follows the relationship described by equation (20.7) and is plotted in figure 20.19(c) for the C-rich side, where values of  $E_g(h\text{-BN}) = 6.4$  eV,  $E_g(\text{C}) = 0$  eV, and the bowing parameter  $b = 4.8$  eV were used. Based on equation (20.7) and figure 20.19(c), a bandgap value of  $E_g = 91$  meV is deduced for the  $h\text{-(BN)}_{1-x}\text{(C}_2)_x$  alloy ( $x = 0.95$ ), which agrees almost perfectly with the value of  $\sim 93$  meV obtained from the temperature dependent carrier concentration presented in the inset of figure 20.19(b) [59]. This excellent agreement between the measured and expected bandgap values provides strong evidence that homogeneous  $h\text{-(BN)}_{1-x}\text{(C}_2)_x$  alloys with  $x \geq 0.95$  have been successfully synthesized using MOCVD at a growth temperature of  $1300$  °C, corroborating well with the conclusion drawn from Raman spectroscopy data shown in figure 20.18.

The temperature dependent free carrier concentration in  $h\text{-(BN)}_{1-x}\text{(C}_2)_x$  epilayers with  $x < 0.95$  has also been measured. The measured thermal activation energies for  $h\text{-(BN)}_{1-x}\text{(C}_2)_x$  epilayers with  $x < 0.95$  are plotted in the inset of figure 20.19(c) and vary from  $\sim 32$  meV to  $\sim 45$  meV. These values significantly deviate from the  $E_g$  versus  $x$  plot shown in figure 20.19(c), which implies that the carrier conduction is no longer intrinsic and that phase separation and formation of separate C–C and B–N domains occurred in the  $h\text{-(BN)}_{1-x}\text{(C}_2)_x$  epilayers with  $x < 0.95$ .

Another unique features of the  $h\text{-(BN)}_{1-x}\text{(C}_2)_x$  alloy system is that it offers the conductivity variation from highly insulating semiconductor (undoped  $h\text{-BN}$ ) to semi-metal (graphite). Figure 20.19(d) shows the measured 300 K electrical resistivity for samples with different carbon concentrations. Both van der Pauw and  $I$ – $V$  characteristic measurements were performed to compare the relative electrical resistivities of  $h\text{-(BN)}_{1-x}\text{(C}_2)_x$  epilayers with varying C concentrations. The results shown in figure 20.19(b) has demonstrated that the electrical resistivity decreases by approximately 15 orders of magnitude when  $x$  increases from 0 to 1 [61]. Since graphite is a semi-metal and undoped  $h\text{-BN}$  is highly insulating, it is expected that when these two systems combine to form  $h\text{-(BN)}_{1-x}\text{(C}_2)_x$  alloys, a large range of electrical conductivity control can be achieved and the electrical conductivity increases with an increase in the C composition. In the phase separated materials, the formation of C clusters further increases the electrical conductivity.

A more recent theoretical study using first-principles *ab initio* calculations combined with a rigorous statistical approach based on cluster expansion was

performed to study the effects of disorder, phase segregation, and composition fluctuations on  $(\text{BN})_{1-x}(\text{C}_2)_x$  monolayer alloy properties [88]. The calculations combined with the generalized quasichemical approximation to account for disorder effects have further confirmed that atomic arrangements with C–C and B–N bonds are energetically favored over the ones with B–B and N–N bonds [88], which further confirmed the simulation results by Yuge [87]. It was found that the most energetically favorable configurations are the atomic arrangements BNBNNBN, CCBNNBN, CCCCNN, CCCCCN, and CCCCCC. The calculated  $T$ - $x$  phase diagram shown in figure 20.20(a) revealed a huge critical temperature  $T_c = 5200$  K, which is comparable to the result of  $T_c = 4500$  K calculated using Monte Carlo simulations, neglecting the lattice vibrations [87]. The calculation results indicated that significant contributions from clusters with B–B and N–N bonds may also occur only at growth temperatures close to the critical temperature. The phase diagram in figure 20.20(a) shows that for normal growth temperatures employed in CVD or MOCVD ( $\sim 1000$  °C) random alloys can only exist for extremely small C composition in the  $h$ -BN-rich side or small  $h$ -BN composition in the C-rich side and that carbon-rich alloys are more thermodynamically favored than  $h$ -BN-rich ones. More specifically, for the growth temperature employed in obtaining  $h$ - $(\text{BN})_{1-x}(\text{C}_2)_x$  alloys shown in figures 20.15–20.19 of  $1300$  °C (or  $T = 1573$  K), the calculation results predicted a very small carbon solubility in  $h$ -BN with a critical carbon composition at  $x_c = 0.028$  and a  $h$ -BN solubility in graphene with a critical carbon composition at  $x_c = 0.958$ . These predication results

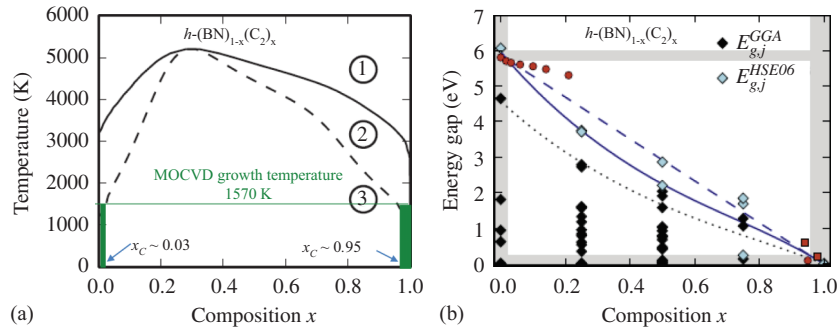


**Figure 20.20.** (a) The  $T$ - $x$  phase diagram of  $h$ - $(\text{BN})_{1-x}(\text{C}_2)_x$ . The bimodal (spinodal) curve is represented by the full (dashed) line. The stable, metastable, and unstable regions in the  $T$ - $x$  diagram are labeled by 1, 2, and 3, respectively. The horizontal line indicates the typical growth temperature employed in MOCVD or CVD growth and the vertical green shaded areas indicate the composition regions where the synthesis of homogeneous  $h$ - $(\text{BN})_{1-x}(\text{C}_2)_x$  alloys has been realized at  $1300$  °C [58–60]. (b) The energy bandgap as a function of the composition for  $h$ - $(\text{BN})_{1-x}(\text{C}_2)_x$  alloys obtained with the GGA functional (dotted black curve) and within the HSE06 approach with and without phase decomposition effects (dashed and solid blue lines, respectively). The vertical gray shades indicate the  $x$  compositions where the alloy is stable and the horizontal ones correspond to the energy gap tune range at the stable composition conditions. The black and light blue diamonds represent the energy bandgap obtained by GGA and HSE06 calculations for the nine most statistically relevant configurations with the lowest excess energies. The experimental data of [58] and [59] (figure 20.16 (b) and 20.19(e)) are represented by red circles and those of [90] are represented by red squares [90]. Reproduced with permission from [88]. Copyright 2017 the American Physical Society.

are in excellent agreement with the experimentally observed values of  $x_c = 0.032$  on the *h*-BN-rich side shown in figures 20.15 and 20.16 and  $x_c = 0.95$  observed on the C-rich side shown in figures 20.18 and 20.19 [58–61].

The same authors have also estimated the structural, electronic, and optical properties within the generalized quasichemical approximation (GQCA) formalism considering a typical growth temperature of  $T = 1600$  K [88]. The simulation results verified that the lattice parameters of the  $h\text{-(BN)}_{1-x}\text{(C}_2\text{)}_x$  alloys follow Vegard's law,  $a(x) = a_{\text{BN}}(1 - x) + a_{\text{C}}x$ ,  $a_{\text{C}} = 2.47$  Å, and  $a_{\text{BN}} = 2.51$  Å and that there is no appreciable layer buckling [88].

Figure 20.20(b) shows the simulated energy bandgap as a function of the carbon composition ( $x$ ) for  $h\text{-(BN)}_{1-x}\text{(C}_2\text{)}_x$  alloys obtained using the generalized gradient approximation (GGA) functional approach as well as the Heyd, Scuseria, and Ernzerhof (HSE06) hybrid functional approach [101] with and without phase decomposition effects, by restricting the electronic structure calculations using the hybrid functional HSE06 to nine most statistically relevant configurations with the lowest excess energies [88]. By assuming that the growth conditions are controlled so that domain sizes are comparable with the considered clusters, including only the composition fluctuation effect, the simulated energy bandgap using the HSE06 approach was shown to vary between  $E_{\text{g}}(h\text{-BN}) = 6.06$  eV and  $E_{\text{g}}(\text{C}) = 0$  eV, following equation (20.7). However, the authors introduced a carbon composition dependent bowing parameter,  $b(x)$ . The calculated bowing parameter is  $b(x) = (5.6 - 4.9x)$  eV [88], which agrees reasonably well with experimental measured values of 3.6 eV in the *h*-BN-rich side shown in figure 20.16(b) [58] and 4.8 eV in the C-rich side shown in figure 20.19(c) [59].

## 20.5 Concluding remarks

Phase separation appears to be a critical issue towards the development of *h*-BN based alloys. Phase separation is a long outstanding issue for InGaN alloys and remains to be solved. Although not much information is available on the phase separation issue in  $h\text{-Ga}_x\text{B}_{1-x}\text{N}$  and  $h\text{-(BN)}_{1-x}\text{(C}_2\text{)}_x$  alloys, the differences between InGaN,  $h\text{-Ga}_x\text{B}_{1-x}\text{N}$ , and  $h\text{-(BN)}_{1-x}\text{(C}_2\text{)}_x$  alloys in terms of phase separation can be briefly summarized as below. Phase separation in InGaN alloys is mainly caused by the difference in the in-plane *a*-lattice constants between InN ( $a = 0.3544$  nm) and GaN ( $a = 0.3189$  nm), whereas the difference in bond energies between B–N (4.0 eV), C–C (3.71 eV), C–N (2.83 eV), and C–B (2.59 eV) is the main cause of the phase separation in  $h\text{-(BN)}_{1-x}\text{(C}_2\text{)}_x$  alloys. On the other hand, phase separation occurs in *h*-GaBN because the stable crystal phases of BN and GaN are hexagonal and wurtzite, respectively.

In addition to the lattice constant mismatch between InN and GaN, the growth temperature mismatch between InN and GaN makes the phase separation issue in InGaN even more difficult to overcome [103]. Theoretically, increasing the growth temperature will reduce the miscibility gap [83, 84, 87, 88], but InN decomposes at high temperatures ( $T > 700$  °C). While the crystalline quality of InGaN alloys can be improved by employing a low growth rate in the low In-content regime [102], growth

conditions farther away from the thermodynamic equilibrium (such as high growth rates) are helpful to promote the formation of single phase InGaN alloys in the theoretically predicted miscibility gap region (the middle range of the alloy composition) [103].

Phase separation is also a significant challenge to the synthesis of homogeneous  $h$ -BN based alloys. However, by combining the results of (BN)-rich  $h$ -(BN) $_{1-x}$ (C $_2$ ) $_x$  and C-rich  $h$ -(BN) $_{1-x}$ (C $_2$ ) $_x$  alloys [58–61], we can conclude that  $h$ -(BN) $_{1-x}$ (C $_2$ ) $_x$  epilayers with  $0.032 < x < 0.95$  are most likely phase separated at a growth temperature of 1300 °C. Recent theoretical calculations performed on monolayer  $h$ -(BN) $_{1-x}$ (C $_2$ ) $_x$  suggests a low solubility of C in BN and BN in graphene at a growth temperature of 1300 °C [87, 88] and shows that the miscibility gap decreases with an increase in the growth temperature [87, 88]. The same trend is expected for  $h$ -GaBN and  $h$ -(BN) $_{1-x}$ (C $_2$ ) $_x$  alloys. The phase diagram for  $h$ -(BN) $_{1-x}$ (C $_2$ ) $_x$  alloys shown in figure 20.20(a) reconstructed from combining the experimental [58, 59] and calculation [88] results can serve as a guideline for the further development of homogeneous  $h$ -(BN) $_{1-x}$ (C $_2$ ) $_x$  alloys. Due to the excellent matches in lattice constants, thermal expansion coefficients, and melting temperatures throughout the entire alloys, it is expected that the alloy miscibility gap in  $h$ -(BN) $_{1-x}$ (C $_2$ ) $_x$  alloys can be reduced or completely removed by increasing the growth temperature. This could be a huge advantage over InGaN in which InN decomposes at high temperatures and a high growth temperature cannot be utilized to close the miscibility gap. It is also expected that the crystalline quality of  $h$ -BN based alloys will be improved at higher growth temperatures. However, theoretical insights concerning possible approaches to overcome the phase separation in  $h$ -Ga $_x$ B $_{1-x}$ N and  $h$ -(BN) $_{1-x}$ (C $_2$ ) $_x$  alloys and the composition dependent electronic properties of epitaxial films are still needed to guide material synthesis.

## Acknowledgement

The research at Texas Tech University (TTU) on  $h$ -Ga $_x$ B $_{1-x}$ N is supported by the US Army Research Office (ARO) (No. W911NF-16-1-0268). The work on  $h$ -(BN) $_{1-x}$ (C $_2$ ) $_x$  was supported by the National Science Foundation (NSF-DMR-1206652). The development of  $h$ -BN material and device technologies at TTU has been supported by DOE ARPA-E (DE-AR0000964), NNSA SSAA program (DE-NA0002927), and (DE-FG02-09ER46552); DHS ARI Program (No. 2011-DN077-ARI048); and NSF (DMR-1206652) and (ECCS-1402886). H X Jiang and J Y Lin are grateful to the AT&T Foundation for the support of Ed Whitacre and Linda Whitacre endowed chairs.

## References

- [1] Maity A, Doan T C, Li J, Lin J Y and Jiang H X 2016 Realization of highly efficient hexagonal boron nitride neutron detectors *Appl. Phys. Lett.* **109** 072101
- [2] Maity A, Grenadier S J, Li J, Lin J Y and Jiang H X 2017 Toward achieving flexible and high sensitivity hexagonal boron nitride neutron detectors *Appl. Phys. Lett.* **111** 033507

- [3] Maity A, Grenadier S J, Li J, Lin J Y and Jiang H X 2018 Hexagonal boron nitride neutron detectors with high detection efficiencies *J. Appl. Phys.* **123** 044501
- [4] Grenadier S J, Maity A, Li J, Lin J Y and Jiang H X 2018 Origin and roles of oxygen impurities in hexagonal boron nitride epilayers *Appl. Phys. Lett.* **112** 162103
- [5] Maity A, Grenadier S J, Li J, Lin J Y and Jiang H X 2019 Effects of surface recombination on the charge collection in *h*-BN neutron detectors *J. Appl. Phys.* **125** 104501
- [6] Maity A, Grenadier S J, Li J, Lin J Y and Jiang H X 2019 High sensitivity hexagonal boron nitride lateral neutron detectors *Appl. Phys. Lett.* **114** 222102
- [7] Grenadier S J, Maity A, Li J, Lin J Y and Jiang H X 2019 Lateral charge carrier transport properties of B-10 enriched hexagonal BN thick epilayers *Appl. Phys. Lett.* **115** 072108
- [8] Jiang H X and Lin J Y 2017 Review—hexagonal boron nitride epilayers: growth, optical properties and device applications *ECS J. Solid State Sci. Technol.* **6** Q3012
- [9] Pantha B N, Dahal R, Nakarmi M L, Nepal N, Li J, Lin J Y, Jiang H X, Paduano Q S and Weyburne D 2007 Correlation between optoelectronic and structural properties and epilayer thickness of AlN *Appl. Phys. Lett.* **90** 241101
- [10] Nakamura S, Fasol G and Pearson S J 2000 *The Blue Laser Diode: The Complete Story* (New York: Springer)
- [11] Kaganer V M, Brandt O, Trampert A and Ploog K H 2005 X-ray diffraction peak profiles from threading dislocations in GaN epitaxial films *Phys. Rev. B* **72** 045423
- [12] Lee S R, West A M, Allerman A A, Waldrip K E, Follstaedt D M, Provencio P P, Koleske D D and Abernathy C R 2005 Effect of threading dislocation on the Bragg peak linewidths of GaN, AlGa<sub>N</sub> and AlN heterolayers *Appl. Phys. Lett.* **86** 241904
- [13] Huang B, Cao X K, Jiang H X, Lin J Y and Wei S H 2012 Origin of the significantly enhanced optical transitions in layered boron nitride *Phys. Rev. B* **86** 155202
- [14] Majety S, Cao X K, Li J, Dahal R, Lin J Y and Jiang H X 2012 Band-edge transitions in hexagonal boron nitride epilayers *Appl. Phys. Lett.* **101** 051110
- [15] Li J, Nam K B, Nakarmi M L, Lin J Y, Jiang H X, Carrier P and Wei S-H 2003 Band structure and fundamental optical transitions in wurtzite AlN *Appl. Phys. Lett.* **83** 5163
- [16] Nam K B, Li J, Nakarmi M L, Lin J Y and Jiang H X 2004 Unique optical properties of AlGa<sub>N</sub> alloys and related ultraviolet emitters *Appl. Phys. Lett.* **84** 5264
- [17] Chen G D, Smith M, Lin J Y, Jiang H X, Wei S-H, Asif Khan M and Sun C J 1996 Fundamental optical transitions in GaN *Appl. Phys. Lett.* **68** 2784
- [18] Li X H *et al* 2015 Demonstration of transverse-magnetic deep-ultraviolet stimulated emission from AlGa<sub>N</sub> multiple-quantum-well lasers grown on a sapphire substrate *Appl. Phys. Lett.* **106** 041115
- [19] Li J, Majety S, Dahal R, Zhao W P, Lin J Y and Jiang H X 2012 Dielectric strength, optical absorption, and deep ultraviolet detectors of hexagonal boron nitride epilayers *Appl. Phys. Lett.* **101** 171112
- [20] Sugino T, Tanioka K, Kawasaki S and Shirafuji J 1997 Characterization and field emission of sulfur-doped boron nitride synthesized by plasma-assisted chemical vapor deposition *Jpn J. Appl. Phys.* **36** L463
- [21] Ioffe Institute, Russia (accessed 17 Jan 2020) <http://ioffe.ru/SVA/NSM/Semicond/>
- [22] Rumyantsev S L, Levinshtein M E, Jackson A D, Mohammmd S N, Harris G L, Spencer M G and Shur M S 2001 *Properties of Advanced Semiconductor Materials GaN, AlN, InN, BN, SiC, SiGe* ed M E Levinshtein, S L Rumyantsev and M S Shur (New York: Wiley) pp 67–92

- [23] Jiang H X and Lin J Y 2014 Hexagonal boron nitride for deep ultraviolet photonic devices *Semicond. Sci. Technol.* **29** 084003
- [24] Nakarmi M L, Kim K H, Khizar M, Fan Z Y, Lin J Y and Jiang H X 2005 Electrical and optical properties of Mg-doped  $\text{Al}_{0.7}\text{Ga}_{0.3}\text{N}$  alloys *Appl. Phys. Lett.* **86** 092108
- [25] Taniyasu Y, Kasu M and Makimoto T 2006 An aluminium nitride light-emitting diode with a wavelength of 210 nanometres *Nature* **441** 325
- [26] Nakarmi M L, Nepal N, Lin J Y and Jiang H X 2009 Photoluminescence studies of impurity transitions in Mg-doped AlGa<sub>N</sub> alloys *Appl. Phys. Lett.* **94** 091903
- [27] Dahal R, Li J, Majety S, Pantha B N, Cao X K, Lin J Y and Jiang H X 2011 Epitaxially grown semiconducting hexagonal boron nitride as a deep ultraviolet photonic material *Appl. Phys. Lett.* **98** 211110
- [28] Majety S, Li J, Cao X K, Dahal R, Pantha B N, Lin J Y and Jiang H X 2012 Epitaxial growth and demonstration of hexagonal BN/AlGa<sub>N</sub> p-n junctions for deep ultraviolet photonics *Appl. Phys. Lett.* **100** 061121
- [29] Jiang H X *et al* 2015 Structures and devices based on boron nitride and boron nitride-III-nitride heterostructures *US Patent #9093581*
- [30] Laleyan D A, Zhao S, Woo S Y, Tran H N, Le H B, Szkopek T, Guo H, Botton G A and Mi Z 2017 AlN/h-BN heterostructures for Mg dopant-free deep ultraviolet photonics *Nano Lett.* **17** 3738
- [31] Arnaud B, Lebe'gue S, Rabiller P and Alouani M 2006 Huge excitonic effects in layered hexagonal boron nitride *Phys. Rev. Lett.* **96** 026402  
Arnaud B, Lebe'gue S, Rabiller P and Alouani M 2008 *Phys. Rev. Lett.* **100** 189702
- [32] Wirtz L, Marini A and Rubio A 2006 Excitons in boron nitride nanotubes: dimensionality effects *Phys. Rev. Lett.* **96** 126104
- [33] Wirtz L, Marini A, Gruning M, Attaccalite C, Kresse G and Rubio A 2008 Comment on huge excitonic effects in layered hexagonal boron nitride *Phys. Rev. Lett.* **100** 189701
- [34] Cao X K, Clubine B, Edgar J H, Lin J Y and Jiang H X 2013 Two-dimensional excitons in three-dimensional hexagonal boron nitride *Appl. Phys. Lett.* **103** 191106
- [35] Doan T C, Li J, Lin J Y and Jiang H X 2016 Bandgap and exciton binding energies of hexagonal boron nitride probed by photocurrent excitation spectroscopy *Appl. Phys. Lett.* **109** 122101
- [36] Nam K B, Li J, Nakarmi M L, Lin J Y and Jiang H X 2003 Deep ultraviolet picosecond time-resolved photoluminescence studies of AlN epilayers *Appl. Phys. Lett.* **82** 1694
- [37] Chen L *et al* 2004 Band-edge exciton states in AlN single crystals and epitaxial layers *Appl. Phys. Lett.* **85** 4334
- [38] Silveira E, Freitas J A Jr, Kneissl M, Treat D W, Johnson N M, Slack G A and Schowalter L J 2004 Near-bandedge cathodoluminescence of an AlN homoepitaxial *Appl. Phys. Lett.* **84** 3501
- [39] Dvorak M, Wei S-H and Wu Z 2013 Origin of the variation of exciton binding energy in semiconductors *Phys. Rev. Lett.* **110** 016402
- [40] Dean C R *et al* 2010 Boron nitride substrates for high-quality graphene electronics *Nat. Nanotechnol.* **5** 722
- [41] Britnell L *et al* 2012 Field-effect tunneling transistor based on vertical graphene heterostructures *Science* **335** 947
- [42] Dean C, Young A F, Wang L, Meric I, Lee G-H, Watanabe K, Taniguchi T, Shepard K, Kim P and Hone J 2012 Graphene based heterostructures *Solid State Commun.* **152** 1275

- [43] Geim A K and Grigorieva I V 2013 Van der Waals heterostructures *Nature* **499** 419
- [44] Tran T T, Elbadawi C, Totonjian D, Lobo C J, Grosso G, moon H, Englund D R, Ford M J, Aharonovich I and Toth M 2016 Robust multicolor single photon emission from point defects in hexagonal boron nitride *ACS Nano*. **10** 7331
- [45] Tran T T, Bray K, Ford M J, Toth M and Aharonovich I 2016 Quantum emission from hexagonal boron nitride monolayers *Nat. Nanotechnol.* **11** 37
- [46] Martínez L J, Pelini T, Waselowski V, Maze J R, Gil B, Cassabois G and Jacques V 2016 Efficient single photon emission from a high-purity hexagonal boron nitride crystal *Phys. Rev. B* **94** 121405(R)
- [47] Jungwirth N R, Calderon B, Ji X, Spencer M G, Flatté M E and Fuchs G D 2016 Temperature dependence of wavelength selectable zero-phonon emission from single defects in hexagonal boron nitride *Nano Lett.* **16** 6052
- [48] Chejanovsky N *et al* 2016 Structural attributes and photodynamics of visible spectrum quantum emitters in hexagonal boron nitride *Nano Lett.* **16** 7037
- [49] Exarhos A L, Hopper D, Grote R R, Alkauskas A and Bassett L C 2017 Optical signatures of quantum emitters in suspended hexagonal boron nitride *ACS Nano*. **11** 3328
- [50] Koperski M, Nogajewski K and Potemski M 2018 Single photon emitters in boron nitride: more than a supplementary material *Opt. Commun.* **411** 158
- [51] Weston L, Wickramaratne D, Mackoite M, Alkauskas A and Van de Walle C G 2018 *Phys. Rev. B* **97** 214104
- [52] Knoll G F 2010 *Radiation Detection and Measurement* 4th edn (New York: Wiley)
- [53] Wang Q W, Uddin M R, Du X Z, Li J, Lin J Y and Jiang H X 2019 Synthesis and photoluminescence properties of hexagonal BGaN alloys and quantum wells *Appl. Phys. Expr.* **12** 011002
- [54] Wang Q W, Li J, Lin J Y and Jiang H X 2019 Critical thickness of hexagonal GaBN/BN heterostructures *J. Appl. Phys.* **125** 205703
- [55] Freeman C L, Claeysens F, Allan N L and Harding J H 2006 Graphitic nanofilms as precursors to wurtzite films: theory *Phys. Rev. Lett.* **96** 066102
- [56] Wu D X, Lagally M G and Liu F 2011 Stabilizing graphitic thin films of wurtzite materials by epitaxial strain *Phys. Rev. Lett.* **107** 236101
- [57] Kecik D, Onen A, Konuk M, Gürbüz E, Ersan F, Cahangirov S, Aktürk E, Durgun E and Ciraci S 2018 Fundamentals, progress and future directions of nitride-based semiconductors and their composites in two-dimensional limit: a first-principles perspective to recent synthesis *Appl. Phys. Rev.* **5** 011105
- [58] Uddin M R, Majety S, Li J, Lin J Y and Jiang H X 2014 Layer-structured hexagonal (BN)C semiconductor alloys with tunable optical and electrical properties *J. Appl. Phys.* **115** 093509
- [59] Uddin M R, Li J, Lin J Y and Jiang H X 2015 Carbon-rich hexagonal (BN)C alloys *J. Appl. Phys.* **117** 215703
- [60] Uddin M R, Doan T C, Li J, Ziemer K S, Lin J Y and Jiang H X 2014 Electrical transport properties of (BN)-rich hexagonal (BN)C semiconductor alloys *AIP Adv.* **4** 087141
- [61] Uddin M R 2016 Epitaxial growth and characterization of hexagonal boron nitride carbon semiconductor alloys *PhD Dissertation* Texas Tech University, Lubbock, TX
- [62] Al Balushi Z Y *et al* 2016 Two-dimensional gallium nitride realized via graphene encapsulation *Nat. Mater.* **15** 1166

- [63] Christopoulos S, Hogersthal G B, Grundy A J D, Lagoudakis P G, Kavokin A V and Baumberg J J 2007 Room-temperature polariton lasing in semiconductor microcavities *Phys. Rev. Lett.* **98** 126405
- [64] Bhattacharya P, Frost T, Deshpande S, Baten M Z, Hazari A and Das A 2014 Room temperature electrically injected polariton laser *Phys. Rev. Lett.* **112** 236802
- [65] Caldwell J D *et al* 2014 Sub-diffractive volume-confined polaritons in the natural hyperbolic material hexagonal boron nitride *Nat. Commun.* **5** 5221
- [66] Honda T, Kurimoto M, Shibata M and Kawanishi H 2000 Excitonic emission of B GaN grown on (0001) 6H-SiC by metal-organic vapor-phase epitaxy *J. Lumin.* **87** 1274
- [67] Wei C H, Xie Z Y, Edgar J H, Zeng H C, Lin J Y, Jiang H X, Chaudhuri J, Ignatiev C and Braski D N 2000 MOCVD growth of GaBN on 6H-SiC (0001) substrates *J. Electron. Mater.* **29** 452
- [68] Polyakov A Y, Shin M, Qian W and Skowronski M 1997 Growth of AlBN solid solutions by organometallic vapor-phase epitaxy *J. Appl. Phys.* **81** 1715
- [69] Akasaka T and Makimoto T 2006 Flow-rate modulation epitaxy of wurtzite AlBN *Appl. Phys. Lett.* **88** 041902
- [70] Li X *et al* 2015 MOVPE grown periodic AlN/AlN heterostructure with high boron content *J. Cryst. Growth* **414** 119
- [71] Li X, Wang S, Liu H, Ponce F A, Detchprohm T and Dupuis R D 2017 100-nm thick single-phase wurtzite AlN films with boron contents over 10% *Phys. Status Solidi B* **254** 1600699
- [72] Zhang M and Li X 2017 Structural and electronic properties of wurtzite  $B_xAl_{1-x}N$  from first-principles calculations *Phys. Status Solidi B* **254** 1600749
- [73] Shen J X, Wickramaratne D and Van de Walle C G 2017 Band bowing and the direct-to-indirect crossover in random AlN alloys *Phys. Rev. Mater.* **1** 065001
- [74] Turiansky M E, Shen J X, Wickramaratne D and Van de Walle C G 2019 First-principles study of bandgap bowing in B GaN alloys *J. Appl. Phys.* **126** 095706
- [75] Hasegawa Y, Akiyama T, Pradipto A M, Nakamura K and Ito T 2018 Empirical interatomic potential approach to the stability of graphitic structure in AlN and B GaN alloys *J. Cryst. Growth* **504** 13
- [76] Hasegawa Y, Akiyama T, Pradipto A M, Nakamura K and Ito T 2019 Theoretical investigations on the structural stability and miscibility in AlN and B GaN alloys: bond-order interatomic potential calculations *Jpn J. Appl. Phys.* **58** SCCB21
- [77] Tusche C, Meyerheim H L and Kirschner J 2007 Observation of depolarized ZnO (0001) monolayers: formation of unreconstructed planar sheets *Phys. Rev. Lett.* **99** 026102
- [78] Museur L and Kanaev A 2008 Near band-gap photoluminescence properties of hexagonal boron nitride *J. Appl. Phys.* **103** 103520
- [79] Silly M G, Jaffrenou P, Barjon J, Lauret J-S, Ducastelle F, Loiseau A, Obraztsova E, Attal-Tretout B and Rosencher E 2007 Luminescence properties of hexagonal boron nitride: cathodoluminescence and photoluminescence spectroscopy measurements *Phys. Rev. B* **75** 085205
- [80] Du X Z, Li J, Lin J Y and Jiang H X 2015 The origin of deep-level impurity transitions in hexagonal boron nitride *Appl. Phys. Lett.* **106** 021110
- [81] Watanabe K, Taniguchi T and Kanda H 2004 Direct-bandgap properties and evidence for ultraviolet lasing of hexagonal boron nitride single crystal *Nature Mater.* **3** 404

- [82] Nemanich R J, Solin S A and Martin R M 1981 Light scattering study of boron nitride microcrystals *Phys. Rev. B* **23** 6348
- [83] Ho I H and Stringfellow G B 1996 Solid phase immiscibility in GaInN *Appl. Phys. Lett.* **69** 2701
- [84] Karpov S Y 1998 Suppression of phase separation in InGaN due to elastic strain *MRS Internet J. Nitride Semicond. Res.* **3** 6
- [85] Van der Merwe J H 1962 Crystal interface. Part II. finite overgrowths *J. Appl. Phys.* **34** 123
- [86] People R and Bean J C 1985 Calculation of critical layer thickness versus lattice mismatch for  $\text{Ge}_x\text{Si}_{1-x}/\text{Si}$  strained-layer heterostructures *Appl. Phys. Lett.* **47** 322
- [87] Yuge K 2009 Phase stability of boron carbon nitride in a heterographene structure: a first-principles study *Phys. Rev. B* **79** 144109
- [88] Guillhon I, Marques M and Teles L K 2017 Optical absorbance and band-gap engineering of  $(\text{BN})_{1-x}(\text{C}_2)_x$  two-dimensional alloys: phase separation and composition fluctuation effects *Phys. Rev. B* **95** 035407
- [89] Ci L *et al* 2010 Atomic layers of hybridized boron nitride and graphene domains *Nature Mater* **9** 430
- [90] Chang C K *et al* 2013 Band gap engineering of chemical vapor deposition graphene by *in situ* BN doping *ACS Nano* **7** 1333
- [91] Gong Y *et al* 2014 Direct chemical conversion of graphene to boron- and nitrogen- and carbon-containing atomic layers *Nat. Commun.* **5** 3193
- [92] Bahandary S and Sanyal B 2012 *Graphene-Boron Nitride Composite: A Material with Advanced Functionalities* (Rijeka: InTech)
- [93] Nozaki H and Itoh S 1996 Structural stability of  $\text{BC}_2\text{N}$  *J. Phys. Chem. Solids* **57** 41
- [94] Watanabe M O, Itoh S, Sasaki T and Mizushima K 1996 Visible-light-emitting layered  $\text{BC}_2\text{N}$  semiconductor *Phys. Rev. Lett.* **77** 187
- [95] Hoffman D M, Doll G L and Eklund P C 1984 Optical properties of pyrolytic boron nitride in the energy range 0.05–10 eV *Phys. Rev. B* **30** 6051
- [96] Dresselhaus M S and Dresselhaus G 2002 Intercalation compounds of graphite *Adv. Phys.* **51** 1
- [97] Reich S and Thomsen C 2004 Raman spectroscopy of graphite *Phil. Trans. R. Soc. Lond. A* **362** 2271
- [98] Meher S R, Biju K P and Jain M K 2011 Raman spectroscopic investigation of phase separation and compositional fluctuations in nanocrystalline  $\text{In}_x\text{Ga}_{1-x}\text{N}$  thin films prepared by modified activated reactive evaporation *Phys. Status Solidi A* **208** 2655
- [99] Semenov G W 1984 Condensed-matter simulation of a three-dimensional anomaly *Phys. Rev. Lett.* **53** 2449
- [100] Razeghi M 2009 *Fundamentals of Solid State Engineering* (Berlin: Springer) ch 7
- [101] Heyd J, Scuseria G E and Ernzerhof M 2003 Hybrid functionals based on a screened Coulomb potential *J. Chem. Phys.* **118** 8207  
Heyd J, Scuseria G E and Ernzerhof M 2006 *J. Chem. Phys.* **124** 219906
- [102] Nakamura S and Fasol G 1997 *The Blue Laser Diode* (Berlin: Springer) pp 201–60
- [103] Pantha B N, Li J, Lin J Y and Jiang H X 2010 Evolution of phase separation in In-rich InGaN alloys *Appl. Phys. Lett.* **96** 232105